The Astrophysical Journal, 806:149 (17pp), 2015 June 20 doi:10.1088/0004-637X/806/2/149


# *NUSTAR* AND *SUZAKU* X-RAY SPECTROSCOPY OF NGC 4151: EVIDENCE FOR REFLECTION FROM THE INNER ACCRETION DISK

M. L. Keck[1], L. W. Brenneman[2], D. R. Ballantyne[3], F. Bauer[4,5,6], S. E. Boggs[7], F. E. Christensen[8], W. W. Craig[7], T. Dauser[9], M. Elvis[2], A. C. Fabian[10], F. Fuerst[11], J. García[2], B. W. Grefenstette[11], C. J. Hailey[12], F. A. Harrison[11], G. Madejski[13], A. Marinucci[14], G. Matt[14], C. S. Reynolds[15], D. Stern[16], D. J. Walton[11,16], and A. Zoghbi[17]

[1] Institute for Astrophysical Research, Boston University, 725 Commonwealth Avenue, Boston, MA 02215, USA; keckm@bu.edu
[2] Harvard-Smithsonian Center for Astrophysics, 60 Garden Street, Cambridge, MA 02138, USA
[3] Center for Relativistic Astrophysics, School of Physics, Georgia Institute of Technology, Atlanta, GA 30332, USA
[4] Instituto de Astrofísica, Facultad de Física, Pontificia Universidad Católica de Chile, 306, Santiago 22, Chile
[5] Millennium Institute of Astrophysics, Vicuña Mackenna 4860, 7820436 Macul, Santiago, Chile
[6] Space Science Institute, 4750 Walnut Street, Suite 205, Boulder, Colorado 80301, USA
[7] Space Sciences Laboratory, University of California, Berkeley, CA 94720, USA
[8] DTU Space, National Space Institute, Technical University of Denmark, Elektrovej 327, DK-2800 Lyngby, Denmark
[9] Dr. Karl Remeis-Observatory and Erlangen Centre for Astroparticle Physics, Sternwartstr. 7, D-96049 Bamberg, Germany
[10] Institute of Astronomy, University of Cambridge, Madingley Road, Cambridge CB3 0HA, UK
[11] Space Radiation Laboratory, California Institute of Technology, Pasadena, CA 91125, USA
[12] Columbia Astrophysics Laboratory, Columbia University, New York, NY 10027, USA
[13] Kavli Institute for Particle Astrophysics and Cosmology, SLAC National Accelerator Laboratory, Menlo Park, CA 94025, USA
[14] Dipartimento di Matematica e Fisica, Università degli Studi Roma Tre, via della Vasca Navale 84, I-00146 Roma, Italy
[15] Department of Astronomy, University of Maryland, College Park, MD 20742-2421, USA
[16] Jet Propulsion Laboratory, California Institute of Technology, Pasadena, CA 91109, USA
[17] Department of Astronomy, University of Michigan, 500 Church Street, Ann Arbor, MI 48109-1042, USA
*Received 2014 September 30; accepted 2015 April 27; published 2015 June 15*

## ABSTRACT

We present X-ray timing and spectral analyses of simultaneous 150 ks *Nuclear Spectroscopic Telescope Array (NuSTAR)* and *Suzaku* X-ray observations of the Seyfert 1.5 galaxy NGC 4151. We disentangle the continuum emission, absorption, and reflection properties of the active galactic nucleus (AGN) by applying inner accretion disk reflection and absorption-dominated models. With a time-averaged spectral analysis, we find strong evidence for relativistic reflection from the inner accretion disk. We find that relativistic emission arises from a highly ionized inner accretion disk with a steep emissivity profile, which suggests an intense, compact illuminating source. We find a preliminary, near-maximal black hole spin $a > 0.9$ accounting for statistical and systematic modeling errors. We find a relatively moderate reflection fraction with respect to predictions for the lamp post geometry, in which the illuminating corona is modeled as a point source. Through a time-resolved spectral analysis, we find that modest coronal and inner disk reflection (IDR) flux variation drives the spectral variability during the observations. We discuss various physical scenarios for the IDR model and we find that a compact corona is consistent with the observed features.

*Key words:* accretion, accretion disks – black hole physics – galaxies: active – galaxies: individual (NGC 4151) – galaxies: Seyfert – X-rays: galaxies

## 1. INTRODUCTION

The dominant features of the X-ray spectra of Seyfert galaxies are a Comptonized continuum, reflection from the accretion disk as well as distant material, and line of sight absorption. Uniquely disentangling these spectral features has been challenging with most X-ray observatories, which primarily have high sensitivity in the $E \sim 0.1-10$ keV band. High sensitivity, broadband (0.5–79 keV) observations of Seyfert galaxies enabled by the *Nuclear Spectroscopic Telescope Array* (*NuSTAR*) (Harrison et al. 2013) combined with observatories with high sensitivity and energy resolution at lower energies, including *Suzaku* (Mitsuda et al. 2007), allow the continuum, reflection, and absorption features to be definitively separated in Seyfert galaxy X-ray spectra. Deconvolving these features can allow for fundamental properties of active galactic nucleus (AGN) coronae, supermassive black holes (SMBHs), and AGN absorption structures to be determined (e.g., NGC 1365, Risaliti et al. 2013; Walton et al. 2014; SWIFT J2127.4+5654, Marinucci et al. 2014a).

The dominant X-ray continuum emission in Seyfert galaxies is commonly thought to be produced by Comptonization of black hole accretion disk thermal emission in a coronal electron plasma (e.g., Haardt et al. 1994; Reynolds & Nowak 2003). The corona could be produced by an accretion disk atmosphere or the base of a jet (e.g., Markoff et al. 2005). Seyfert galaxies can produce weak jets even though they are radio quiet (Ghisellini et al. 2004). For some AGNs, the corona is compact with a characteristic distance from the accretion disk $D \lesssim 10\ r_g$ (where $r_g \equiv GM/c^2$) as inferred from X-ray micro-lensing, reverberation, and eclipse measurements (e.g., Chartas et al. 2009; Zoghbi et al. 2012; Reis & Miller 2013; Sanfrutos et al. 2013 and references therein). Because of the compact sizes inferred for AGN coronae, their detailed geometry has been difficult to determine.

Coronal emission is reprocessed in the black hole accretion disk, which primarily produces relativistically skewed fluorescent Fe K$\alpha$ line emission (rest-frame energy $E = 6.4$ keV for neutral Fe) and a Compton scattering "hump" at energies $E \gtrsim 10$ keV (e.g., Fabian et al. 1989; George & Fabian 1991).

Through measuring the relativistic distortion of the inner accretion disk reflection, important properties of the inner accretion disk and black hole can be determined, including the black hole spin (Brenneman 2013; Reynolds 2013, and references therein). SMBH spin (which has dimensionless form $a \equiv cJ/GM^2$ where $J$ and $M$ are the black hole angular momentum and mass, respectively) encodes the accretion and merger history of a SMBH (Berti & Volonteri 2008). Building upon the census of the ∼22 SMBH spin measurements currently in the literature (e.g., Brenneman 2013; Reynolds 2013; Walton et al. 2013, and references therein) is crucial for understanding SMBH evolution. SMBH spin also likely plays a critical role in driving AGN outflows and jets that deposit matter and energy in their environment (e.g., Fabian 2012).

Nuclear emission is absorbed in several regions commonly associated with ionized outflows (e.g., Elvis 2000), the broad-line region (Antonucci 1993; Urry & Padovani 1995), and/or a molecular torus (e.g., Krolik & Begelman 1988). Absorption and relativistic reflection can produce similar spectral features in the Fe K band. This has led some authors to suggest that the relativistic reflection features actually arise purely from absorption and Compton scattering in material relatively far from the black hole where relativistic effects are negligible (e.g., Miller et al. 2009).

The Seyfert 1.5 galaxy NGC 4151 ($z = 0.00332$, de Vaucouleurs et al. 1991), which is sometimes considered to be the archetypical Seyfert 1 galaxy, is a source in which many AGN phenomena were first characterized (for a review, see Ulrich 2000). The source has bolometric luminosity $L_{\rm bol} \sim 5 \times 10^{43}$ erg s$^{-1}$ (Woo & Urry 2002), SMBH mass $M = 4.57^{+0.57}_{-0.47} \times 10^7\ M_\odot$ from optical and UV reverberation (Bentz et al. 2006), and corresponding Eddington ratio $L_{\rm bol}/L_{\rm Edd} \sim 0.01$. Despite being one of the brightest and most studied AGNs, few constraints on the coronal geometry and the black hole spin have been found for the source.

NGC 4151 has a harder X-ray continuum relative to the average Seyfert AGN. If approximated with a power law, it has a photon index historically measured to be in the range $\Gamma \sim 1.3$–$1.9$ (e.g., Ives et al. 1976; Perola et al. 1986; Yaqoob & Warwick 1991; Zdziarski et al. 1996; Piro et al. 1999; Beckmann et al. 2005). NGC 4151 was also the first AGN in which a high-energy cutoff was clearly detected (Jourdain et al. 1992, *SIGMA*; Maisack et al. 1993, *CGRO* OSSE). From an analysis of all *INTEGRAL* data of the source and data from other X-ray observatories during the period 2003 January to 2009 June, Lubiński et al. (2010) found that the coronal emission had an approximately constant X-ray spectral index and Compton $y$ parameter and inferred that the corona had an approximately constant geometry. The X-ray continuum conceivably could arise in the base of a jet, as NGC 4151 has displayed a non-relativistic jet as observed using radio interferometry (Wilson & Ulvestad 1982; Mundell et al. 2003; Ulvestad et al. 2005) and characterized using optical (e.g., Storchi-Bergmann et al. 2009) and X-ray observations (e.g., Wang et al. 2011a, *Chandra* ACIS).

NGC 4151 has shown inconsistent evidence for reflection from the inner accretion disk from X-ray spectroscopy. Spectral analyses of observations taken with instruments with a $E \sim 0.1$–$10$ keV bandpass and CCD resolution have indicated the presence of relativistic reflection in NGC 4151 (e.g., Yaqoob et al. 1995, ASCA; Nandra et al. 2007, *XMM-Newton*). However, other analyses find no such evidence for it (e.g., Schurch et al. 2003, *XMM-Newton*; Patrick et al. 2012, *Suzaku*+*Swift*). The lack of simultaneous broadband ($E \sim 1$–$100$ keV), high-sensitivity X-ray observations of NGC 4151 combined with the complex absorption (total $N_{\rm H} \sim 10^{23}$ cm$^{-2}$) and soft emission (e.g., Armentrout et al. 2007; Wang et al. 2011b) in the source have also made the unambiguous detection of relativistic reflection challenging.

Recent X-ray reverberation studies of eight archival *XMM-Newton* observations have shown that NGC 4151 has a compact corona surrounding a near-maximally rotating black hole. The discovery of Fe K$\alpha$ reverberation in NGC 4151 by Zoghbi et al. (2012) indicates the presence of broad Fe K$\alpha$ line emission that responds to coronal emission originating from a height above the accretion disk on the order of a few $r_g$. A more recent Fe K$\alpha$ reverberation analysis by Cackett et al. (2014) shows evidence supporting a maximally spinning ($a = 0.998$) black hole compared to a low spin black hole ($a = 0.1$) and an illuminating source characterized by the lamp post geometry (in which the corona is modeled as a point source on the spin axis; Martocchia et al. 2002; Miniutti et al. 2003) with height $h = 7.0^{+2.9}_{-2.6}\ r_g$ ($1\sigma$ errors are given).

On larger scales, NGC 4151 exhibits partial-covering, neutral material (e.g., Holt et al. 1980) and ionized outflows (e.g., Wang et al. 2011b and references therein) viewed in absorption. The source has displayed absorption column density variability on timescales as short as $\Delta t \sim 2$ days, which indicates that the absorbing material is located in the broad-line region (de Rosa et al. 2007; Puccetti et al. 2007). The absorption has also been characterized as having an ionized[18] ($\xi \sim 500$ erg cm s$^{-1}$), outflowing ($v_{\rm out} \sim 500$ km s$^{-1}$) component suggestive of an accretion disk wind (*Chandra* HETG; Kraemer et al. 2005) as well as a highly ionized ($\xi \sim 10^4$–$10^5$erg cm s$^{-1}$) and blueshifted ($v_{\rm out} \sim 0.1c$) "ultra-fast outflow" component that might be associated with an accretion disk wind or a weak jet (Tombesi et al. 2011).

In this paper, we present timing and spectral analyses of simultaneous 150 ks *NuSTAR* and *Suzaku* X-ray observations of NGC 4151 in a moderately bright state focused on deconvolving the continuum, reflection, and absorption features. In a separate paper, we will present a reverberation analysis of these observations (A. Zoghbi et al. 2015, in preparation). This paper is structured as follows: Section 2 summarizes the observations and data reduction; Section 3 discusses the timing analysis; Section 4 presents time-averaged (Section 4.1) and time-resolved (Section 4.2) spectral analyses; Section 5 discusses systematic errors and the physical implications of our results; and Section 6 presents our conclusions.

## 2. OBSERVATIONS AND DATA REDUCTION

*Suzaku* and *NuSTAR* observed NGC 4151 from 2012 November 11–14. *Suzaku* observations were taken with NGC 4151 placed at the nominal X-ray Imaging Spectrometer (XIS) pointing position. The *Suzaku* observation has the observation ID 707024010, and the *NuSTAR* observation is composed of three pointings with observation IDs 60001111002, 60001111003, and 60001111005. *Suzaku* and *NuSTAR*

[18] Ionization is parameterized with the ionization parameter, which is defined as the ratio of the ionizing X-ray flux to the gas density: $\xi \equiv \frac{4\pi F_x}{n}$.

**Table 1**
*Suzaku* and *NuSTAR* Observation Information

| Instrument | Band[a] (keV) | Time (ks) | Count Rate (cts $s^{-1}$) | Counts |
|---|---|---|---|---|
| *Suzaku* XIS-0 + 3 | 2.5–9 | 150 | 6.180 ± 0.007 | 929099 |
| *Suzaku* XIS-1 | 2.5–7.5 | 150 | 2.444 ± 0.004 | 367408 |
| *Suzaku* PIN | 14–60 | 141 | 0.985 ± 0.003 | 138881 |
| *NuSTAR* FPMA[b] | 5–79 | 141 | 5.154 ± 0.006 | 723597 |
| *NuSTAR* FPMB[b] | 5–79 | 141 | 4.915 ± 0.006 | 690323 |

**Notes.** Counts and count rates are background subtracted.
[a] Column gives energy bands used in the spectral analysis.
[b] *NuSTAR* data corresponds to the co-added *NuSTAR* observations.

observation information is given in Table 1. Source and background spectra provide a source-dominated view of the 2.5–79 keV emission from NGC 4151 as shown in Figure 1. We reprocessed all data using `HEAsoft` version 6.16, which includes `XSPEC` v12.8.2 (Arnaud 1996) and `xronos` v5.22.

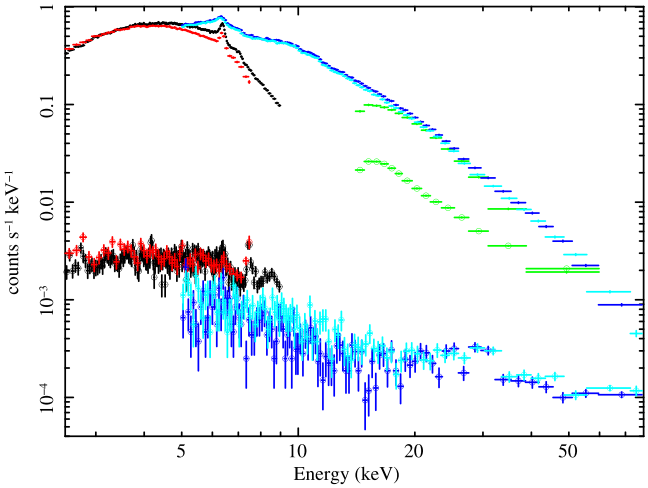


**Figure 1.** Source and background spectra for the XIS-FI (shown in black), XIS-1 (red), PIN (green), FPMA (blue), and FPMB (light blue) instruments. Source count rates are marked with error bars, and background count rates are marked with error bars in circles. For all instruments, source count rates exceed background count rates except for the PIN instrument above $E \sim 40$ keV.

### 2.1. *Suzaku*

We produced *Suzaku* data from the XIS (Koyama et al. 2007) (XIS 0, XIS 1, and XIS 3) using the `aepipeline` script following the *Suzaku* ABC Guide[19] with version 22 of the *Suzaku* software and the XIS `CALDB` release of 2015 January 5, which includes updated XIS gain files. We extracted *Suzaku* XIS data products (i.e., spectra, response files, and light curves) using `xselect` and `xisresp` from circular, 170″ radius regions centered on the source. For each observation, background spectra were extracted from as much of the chip as possible. Source and background regions excluded all contaminating sources in the field of view (primarily the BL Lac object 1E1207.9+3945 and the LINER NGC 4156) and calibration sources in the corners of the chip.

We rebinned *Suzaku* XIS spectra and response files from 4096 to 2048 channels to expedite spectral fitting without compromising the energy resolution of the data. We then co-added data from the XIS front-illuminated (XIS-FI) instruments, XIS 0 and XIS 3, using the `addascaspec` script to maximize signal-to-noise ratio (S/N). We rebinned XIS source spectra into channels with a minimum of 25 counts per bin using `grppha` to allow for robust $\chi^2$ fitting. In the spectral analysis, we apply a cross-normalization constant to all detectors relative to the co-added XIS-FI data. XIS-1 fits with a cross-normalization of 0.96 ± 0.01, which is lower than the nominal XIS-1/XIS-FI cross-normalization[20], 1.019 ± 0.010. However, our value is reasonable given that the cross-normalization depends on the exact spectral shape of the source and exactly where the source is on the chip (K. Mukai 2015, private communication).

Because *Suzaku* and *NuSTAR* observed NGC 4151 in a relatively bright state, we assessed the influence of pileup in the XIS data (note that *NuSTAR* does not suffer from pileup) using the `pileest` script. We found that, for XIS 0, 1, and 3, the central ~30″ has a pileup fraction $3\% \lesssim f_{\rm pl} \lesssim 10\%$ assuming a grade migration parameter of 0.5. We found that this minor pileup fraction does not influence our conclusions in the timing and spectral analyses on the spectral properties of NGC 4151 as described in the Appendix.

We reprocessed the *Suzaku* Hard X-ray Detector (HXD) PIN instrument (Takahashi et al. 2007) data using the `aepipeline` script with the 2011 September 15 HXD calibration files. We reduced and extracted it following the *Suzaku* ABC Guide (see footnote 19). We estimated the PIN non-X-ray background (NXB) using the version 2.2 "tuned" NXB event file for 2012 November as well as response and flat-field files for epoch 11 data. We estimated the PIN cosmic X-ray background with `XSPEC` simulations using the model of Boldt (1987). We rebinned PIN data to a S/N of 5 using `ISIS` (Houck & Denicola 2000) to facilitate $\chi^2$ fitting. Three percent systematic errors were added to PIN data as recommended by the *Suzaku* team to account for uncertainties present in the NXB data. We allow the cross-normalization factor of PIN relative to the XIS-FI instruments to vary in the spectral analysis to improve upon the agreement between the PIN and FPMA/FPMB spectra found with the nominal value (see footnote 20), 1.164 ± 0.014. It fits to 1.26 ± 0.01.

### 2.2. *NuSTAR*

We reprocessed *NuSTAR* focal plane module A and B (FPMA and FPMB) data using the *NuSTAR* Data Analysis Software (`NuSTARDAS`) version 1.4.1, using the *NuSTAR* `CALDB` from 2014 July 1. `NuSTARDAS` performs standard data calibration and data screening, including the elimination of data collected when the earth occulted NGC 4151 and when *NuSTAR* was in the South Atlantic Anomaly. For each of the *NuSTAR* observations, we extracted source data products from a 70″ radius circular region centered on NGC 4151, and we extracted background spectra from 70″ radius circular regions on the same detector chosen to avoid contamination and detector edges. Background regions were separated by at least 4′ from NGC 4151 and ≳7′ from 1E1207.9+3945 and NGC 4156, which exclude ≳98% and ≳99% of the enclosed counts for a point source, respectively (Harrison et al. 2013). Spectra from the three *NuSTAR* observations were co-added and

[19] http://heasarc.gsfc.nasa.gov/docs/suzaku/analysis/abc/
[20] http://heasarc.gsfc.nasa.gov/docs/suzaku/analysis/watchout.html

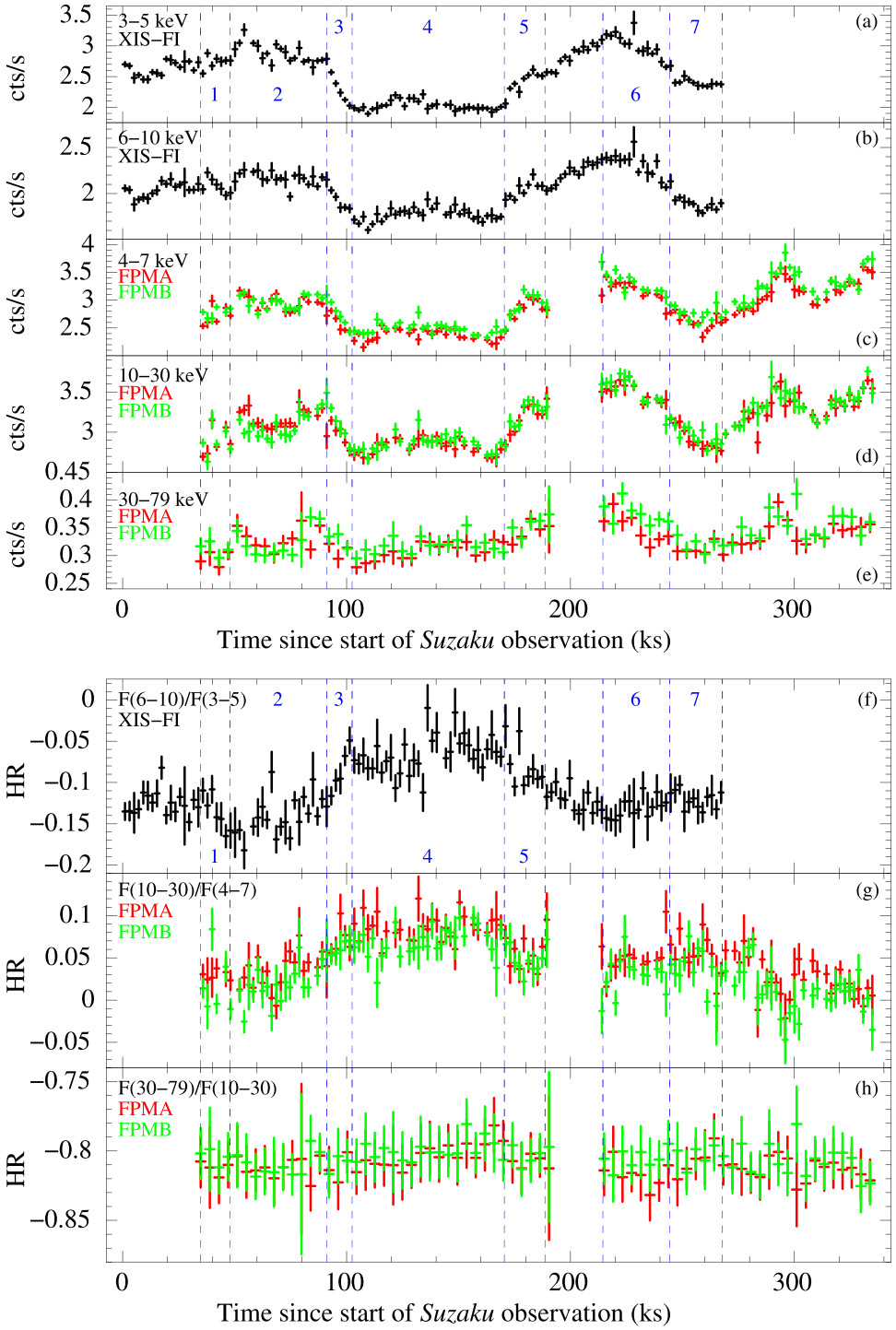


**Figure 2.** Light curves and hardness ratios with 2048 s bins (except for panels (e) and (h), which are shown with 4096 s bins to better show the variability of the 30–79 keV flux). Note the reduction in the broadband flux coincident with a general increase in spectral hardness seen during a $\Delta t \sim 15$ ks period labeled interval 3. Panels (a) and (b) show the *Suzaku* XIS-FI 3–5 keV and 6–10 keV light curves as labeled. Panels (c)–(e) show *NuSTAR* light curves in the 4–7 keV, $10-30$ keV, and $30-79$ keV bands, respectively. Panels (f)–(h) show the hardness ratios $F\,(6-10\,\mathrm{keV})/F\,(3-5\,\mathrm{keV})$, $F\,(10-30\,\mathrm{keV})/F\,(4-7\,\mathrm{keV})$, and $F\,(30-79\,\mathrm{keV})/F\,(10-30\,\mathrm{keV})$, respectively. Vertical blue dashed lines indicate time intervals 1–7 analyzed in the time-resolved analysis as numbered.

analyzed separately for FPMA and FPMB. We rebinned FPMA and FPMB spectra into channels with a minimum S/N of 5 to allow for $\chi^2$ fitting. We allow the FPMA and FPMB cross-normalization constants relative to XIS-FI to fit freely in the spectral analysis, and they fit to $1.04 \pm 0.01$ and $1.08 \pm 0.01$, respectively.

## 3. TIMING ANALYSIS

The *Suzaku* XIS and *NuSTAR* light curves and hardness ratios (HRs) have small but significant variability as shown in Figure 2. Notably, a drop in flux coincident with an increase in spectral hardness is seen during a $\Delta t \sim 15$ ks period labeled interval 3. During interval 3, the 3−5 keV flux

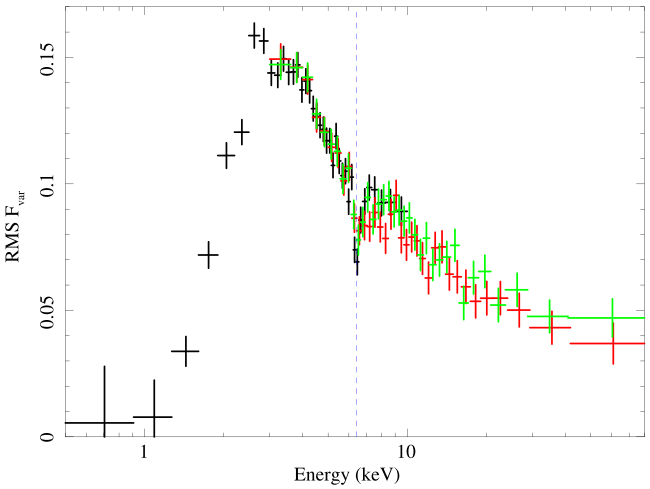


**Figure 3.** The rms fractional variability of the data calculated with 4000 s bins. XIS-FI is in black, FPMA is red, and FMPB is green (XIS-1 is not shown for clarity). Data are included in the energy range 0.7–10 keV for XIS-FI and 3–79 keV for FPMA and FPMB. The dashed blue line indicates the rest-frame energy of the neutral Fe K$\alpha$ emission line (6.4 keV).

drops by a factor of ∼1.4 and the 10–30 keV flux decreases by a factor of ∼1.2. At the same time, the HR between the 6–10 keV flux and the 3–5 keV flux increases by ∼5$\sigma$. Between intervals 4 and 6 ($\Delta t \sim 45$ ks), the 3–5 keV flux rises by a factor of ∼1.6, the 10–30 keV flux increases by a factor of ∼1.3, and the $F(6-10\,\mathrm{keV})/F(3-5\,\mathrm{keV})$ HR decreases by ∼4$\sigma$. From the beginning of interval 6 to the end of interval 7 ($\Delta t \sim 40$ ks), the 3–5 keV flux drops by a factor of ∼1.4, the 30–79 keV flux decreases by a factor of ∼1.3, and the $F(6-10\,\mathrm{keV})/F(3-5\,\mathrm{keV})$ HR remains approximately constant.

The rms fractional variability (rms $F_{\mathrm{var}}$) is shown in Figure 3. The overall source variability drops dramatically below $E \sim 3$ keV, where circumnuclear and scattered emission dominate the absorbed emission from the AGN (e.g., Wang et al. 2011b). There is also an overall drop in variability with increasing energy above $E \sim 3$ keV, which is typical of Seyfert AGNs, where the more variable model components tend to dominate at softer energies. The sharp, relatively narrow dip at 6.4 keV is an indication that the neutral, narrow component of the Fe K$\alpha$ line is not varying much relative to the surrounding continuum during the observation. This is expected of the neutral, narrow reflection component because it likely originates relatively far from the nucleus.

## 4. SPECTRAL ANALYSIS

We perform time-averaged and time-resolved analyses to characterize the broadband X-ray spectral features and variability of NGC 4151. We first undertake a time-averaged spectral analysis (i.e., jointly fitting the full XIS-FI, XIS-1, PIN, FPMA, and FPMB spectra) to understand the components present in the source spectrum using the high S/N of the full data. We then carry out a time-resolved analysis to characterize spectral variability that is averaged out in the full observations, which may include variations in the coronal emission (which can vary on hour-long timescales in AGN; e.g., Markoff et al. 2005), the inner accretion disk reflection emission (which can vary on the order of hours in NGC 4151; e.g., Zoghbi et al. 2012) and absorption features (which can vary on the order of days in NGC 4151; e.g., Puccetti et al. 2007).

To carry out the spectral analyses, we use `XSPEC` with a standard cosmology of $H_0 = 70$ km s$^{-1}$ Mpc$^{-1}$, $\Omega_M = 0.27$, and $\Omega_\Lambda = 0.73$ (Komatsu et al. 2011). We use X-ray cross-section values from Verner et al. (1996) and solar abundance values from Wilms et al. (2000). We include data in the energy ranges indicated in Table 1.

For the spectral analysis, we apply an inner disk reflection (IDR) model and an absorption-dominated model. In brief, the IDR model includes a partial-covering, neutral absorption component (which we refer to as PC1), a distant reflection component (DRC), a cut-off power-law component (PLC), and an IDR component. The absorption-dominated model is identical to the IDR model except that the IDR component is replaced with another partial-covering absorber (PC2). For the time-averaged analysis, we link all parameters between data sets, and we fix redshifts of all model components to the systemic redshift. We model Milky Way absorption with `Tbabs` (Wilms et al. 2000), and we fix the Milky Way absorption column density to the weighted-average value for NGC 4151 from the LAB survey (Kalberla et al. 2005), $N_{\mathrm{H}} = 2.3 \times 10^{20}$ cm$^{-2}$ . We determine 90% confidence intervals for one interesting parameter for all parameter values presented in the time-averaged and time-resolved analyses using the `XSPEC` error algorithm unless noted otherwise.

### 4.1. Time-averaged Analysis

To develop the time-averaged model, we first characterize the continuum absorption and emission features in the 2.5–4.0 keV, 7.5–10 keV, and 50–79 keV bands. We model the coronal continuum emission with a cut-off power law with photon index $\Gamma$ and cut-off fixed at $E_{\mathrm{cut}} = 1000$ keV. Data/model ratios in Figure 4 illustrate the presence of a strong absorption cut-off at energy $E \sim$ 2–3 keV, indicative of a relatively high line of sight column density ($N_{\mathrm{H}} \sim 10^{23}$cm$^{-2}$ ) as well as a prominent, narrow Fe K$\alpha$ emission line at 6.4 keV and Compton hump indicative of reflection.

We apply a partial-covering, neutral absorption component (`partcov* zTbabs`; Wilms et al. 2000). This absorber greatly improves the fit (see Table 2) and satisfactorily accounts for the low-energy continuum ratios as shown in Figure 4. We then model the prominent, narrow Fe K$\alpha$ emission line and Compton hump as arising by reflection of cut-off power-law emission from Compton-thick, plane-parallel, and relatively neutral (i.e., $\xi = 1$ erg cm s$^{-1}$) material with the `xillver` reflection model (García et al. 2013). We specifically employ `xillver-Ec3`[21], which allows for a variable cut-off energy in the range $E = 20$–1000 keV. We fix the incident cut-off power-law photon index and cut-off energy of this component self-consistently to those of the cut-off PLC, and we additionally fix its inclination to $i = 60°$. As shown in the bottom panels of Figure 4, the added `xillver` component significantly reduces the ratios toward unity. The remaining residuals indicate the presence of blended Fe XXV and Fe XXVI K$\alpha$ ($E = 6.67$ keV and $E = 6.97$ keV, respectively) and K$\beta$ ($E = 7.88$ keV and $E = 8.25$ keV, respectively) absorption lines as well as broad emission in the Fe K band and convex curvature above $E \sim 10$ keV.

[21] available at http://hea-www.cfa.harvard.edu/~javier/xillver/

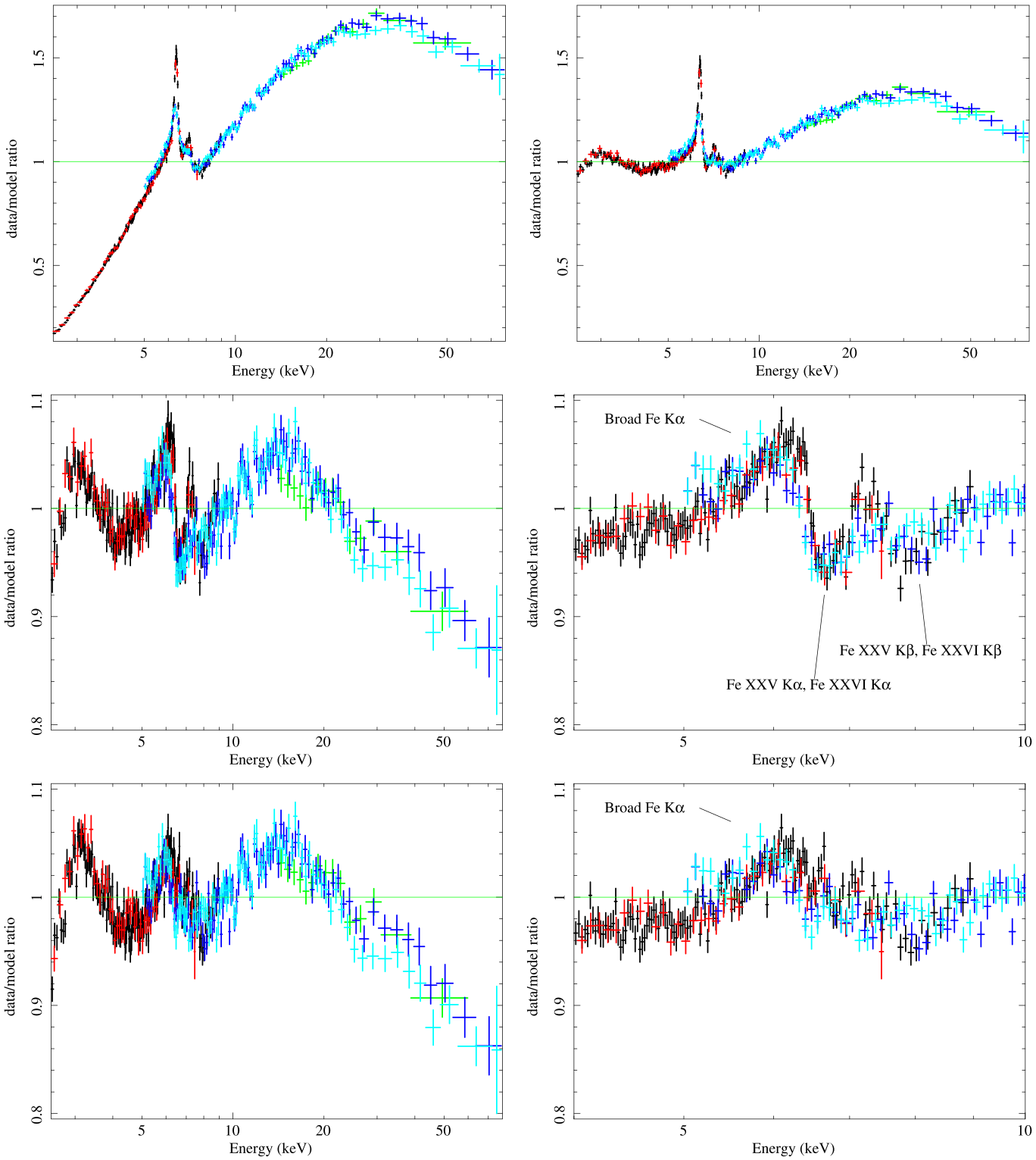


**Figure 4.** Top left: data/model ratios of a power law ($\Gamma = 1.75$) absorbed only by gas in the Milky Way that demonstrate the strong absorption in the source. Top right: data/model ratios after adding a partial covering, neutral absorber and refitting that show the spectral features of relatively neutral reflection. Middle left: best-fit ratios after additionally including a neutral reflection component with free Fe abundance and refitting with $\Gamma = 1.75$ fixed. Middle right: same as middle left, focused on the ratios in the 4–10 keV band. Notice the probable broad Fe K$\alpha$ line as well as the blended Fe XXV and Fe XXVI absorption lines. Bottom Left: best-fit ratios after additionally including two warm absorber components and refitting with $\Gamma = 1.75$ fixed. Bottom right: same as bottom left, focused on the ratios in the 4–10 keV band. For plotting purposes only, spectral bins have either a significance of 80$\sigma$ or a maximum of 80 spectral channels for each panel. Also, XIS-FI data is black, XIS-1 is red, PIN is light green, FPMA is dark blue, and FPMB is light blue.

**Table 2**
$\chi^2$ and $\nu$ After the Addition of Each Time-averaged Model Component

| Additional component | $\chi^2$ | $\nu$ | $\chi^2/\nu$ |
|---|---|---|---|
| Cut-off power law | 264344 | 4120 | 64.2 |
| Partial-covering absorber | 15626 | 4118 | 3.80 |
| Distant reflector[a] | 6264 | 4112 | 1.52 |
| Warm absorber 1 | 5581 | 4110 | 1.36 |
| Warm absorber 2 | 5513 | 4108 | 1.34 |
| Inner disk reflector | 4453 | 4101 | 1.09 |

**Note.** Each added model component provides a significant improvement to the fit.
[a] Values includes a change $\Delta\chi^2/\Delta\nu = -39/-4$ from allowing the instrument cross-normalizations to fit freely.

To account for the unmodeled absorption lines in the Fe band, we additionally apply two separate XSTAR absorption table models, which we refer to as warm absorbers one (WA1) and two (WA2). WA1 is parameterized by its column density in the range $N_{\rm H} = 10^{22}$–$10^{24}$ cm$^{-2}$ and ionization parameter $\xi$ in the range $\log(\xi/{\rm erg\ cm\ s^{-1}}) = 2.5$–$4.5$. The absorber has turbulent velocity $v_t = 3000$ km s$^{-1}$, which is appropriate for a highly ionized absorber (Tombesi et al. 2011). We fix the Fe abundance to one. WA2 is parameterized by its column density in the range $N_{\rm H} = 10^{20}$–$10^{24}$ cm$^{-2}$ and $\xi$ in the range $\log(\xi/{\rm erg\ cm\ s^{-1}}) = 0.0$–$4.0$. It has a turbulent velocity $v_t = 200$ km s$^{-1}$. The Fe abundance is hard-wired at one. We limit $\xi$ to be in the range $\log(\xi/{\rm erg\ cm\ s^{-1}}) = 2.5$–$4.0$. For both WA1 and WA2, $\xi$ is sampled with resolution $\Delta\log(\xi/{\rm erg\ cm\ s^{-1}}) = 0.2$, which is important for accurately modeling the absorption opacities and consequently determining the black hole spin (Reynolds et al. 2012). Having accounted for these spectral features, we develop separate IDR and absorption-dominated models to account for the remaining broad residuals.

#### 4.1.1. IDR Model

We first characterize the broad residuals in the Fe K-band phenomenologically. We begin by applying a broad Gaussian. The line fits with equivalent width ${\rm EW} = 66^{+16}_{-15}$ eV, $\sigma = 0.39 \pm 0.04$ keV, and line energy $E = 6.20 \pm 0.05$ keV. The fit improves by $\Delta\chi^2/\Delta\nu = -341/-3$. The measured line energy and width are suggestive of broadened Fe K$\alpha$ emission. To test for an origin from the inner accretion disk, we replace the Gaussian with a model of line emission from the inner accretion disk (relline; Dauser et al. 2010) with an emissivity profile $\epsilon \propto r^{-q}$ with $q = 3$ fixed. The relline component fits with line energy $E = 6.52 \pm 0.01$ keV, $EW = 111^{+16}_{-22}$ eV, inclination $i = 6 \pm 1°$, and spin $a > 0.99$. The addition of the broad Fe line is statistically motivated by a reduction in $\chi^2$ by $\Delta\chi^2/\Delta\nu = -354/-4$.

To account for emission from the inner accretion disk self-consistently (i.e., by including the full reflection spectrum, including the Compton hump, Fe K$\alpha$ and K$\beta$ emission lines, and the Fe K absorption edge), we include an IDR component composed of the xillver model convolved with the relconv relativistic convolution model (Dauser et al. 2010). Specifically, we use an optimized version relconvf (J. Sanders, private communication). relconv allows the black hole spin, $a$, to fit freely in the range $-0.998 \leqslant a \leqslant 0.998$. We further allow the IDR to have a broken power-law emissivity profile that transitions from inner emissivity index $q_1$ to outer emissivity index $q_2$ at a radius $r_{\rm br}$. relconv additionally assumes an inner accretion disk that is geometrically thin, optically thick, and aligned perpendicular to the spin axis.

We assume that the inner disk radius ($r_{\rm in}$) is fixed at the innermost stable circular orbit (ISCO) radius and that the outer disk radius is fixed at $r_{\rm out} = 400\ r_g$. This value should be unconstrained assuming $q_2 \gtrsim 3$ as expected for rapidly spinning black holes (e.g., Wilkins & Fabian 2011). We assume an isotropic emission distribution as discussed in Svoboda et al. (2009). We further assume that the AGN is chemically homogeneous as discussed in, e.g., Reynolds et al. (2012) and Walton et al. (2013), so we fix the Fe abundances of the distant reflector and IDR together. We additionally limit the Fe abundance to be in the range $0.5 < A_{\rm Fe} < 5.0$ in order to keep the Fe abundance within the range measured for relatively neutral gas in the source (Yaqoob et al. 1993; Schurch et al. 2003; Nandra et al. 2007). We are also motivated to do

**Table 3**
Time-averaged Spectral Analysis Best-fit Values for the Inner Disk Reflection Model

| Component | Parameter (Units) | Values |
|---|---|---|
| Partial covering | $N_{\rm H}$ (cm$^{-2}$) | $(15.4 \pm 0.6) \times 10^{22}$ |
| (partcov* zTbabs) | $f_{\rm cov}$ | $0.92 \pm 0.01$ |
| Warm absorber 1 | $N_{\rm H}$ (cm$^{-2}$) | $2.8^{+0.5}_{-0.3} \times 10^{22}$ |
| (XSTAR grid) | $\log(\xi/{\rm erg\ cm\ s^{-1}})$ | $2.5^{+0.1}_{-0.0p}$ |
| Warm absorber 2 | $N_{\rm H}$ (cm$^{-2}$) | $2.4^{+0.5}_{-0.6} \times 10^{22}$ |
| (XSTAR grid) | $\log(\xi/{\rm erg\ cm\ s^{-1}})$ | $3.3 \pm 0.1$ |
| Distant reflector | $A_{\rm Fe}$ | $5.0^{+0.0p}_{-0.1}$ |
| (xillver) | $K_{\rm DRC}$ (ph cm$^{-2}$ s$^{-1}$) | $(1.7 \pm 0.1) \times 10^{-4}$ |
| Cut-off power law | $\Gamma$ | $1.75^{+0.01}_{-0.02}$ |
| | $E_{\rm cut}$(keV) | $1000(f)$ |
| | $K_{\rm PLC}$ (ph cm$^{-2}$ s$^{-1}$) | $3.7^{+0.4}_{-0.3} \times 10^{-2}$ |
| Inner disk reflection | $a$ | $0.98 \pm 0.01$ |
| (relconvf* xillver) | $q_1$ | $10.0^{+0.0p}_{-0.4}$ |
| | $q_2$ | $2.9 \pm 0.1$ |
| | $r_{\rm br}$ ($r_g$) | $3.3 \pm 0.1$ |
| | $r_{\rm in}$ | $r_{\rm ISCO}$ $(f)$ |
| | $r_{\rm out}$ ($r_g$) | 400 $(f)$ |
| | $\log(\xi/{\rm erg\ cm\ s^{-1}})$ | $3.07 \pm 0.02$ |
| | $i$ (degree) | $18^{+2}_{-0p}$ |
| | $K_{\rm IDR}$ (ph cm$^{-2}$ s$^{-1}$) | $(1.3 \pm 0.1) \times 10^{-6}$ |
| Cross-normalization[a] | XIS-1 | $0.96 \pm 0.01$ |
| | PIN | $1.26 \pm 0.01$ |
| | FPMA | $1.04 \pm 0.01$ |
| | FPMB | $1.08 \pm 0.01$ |
| Flux, absorbed[b] | $F_{2-10}$ (erg cm$^{-2}$ s$^{-1}$) | $1.50 \times 10^{-10}$ |
| Fit | $\chi^2/\nu$ | 4453/4101 (1.09) |

**Notes.** Statistical errors are quoted to 90% confidence for one interesting parameter. The redshifts of all components of the source are fixed to the systemic value, $z = 0.00332$. The Fe abundances of the IDR and distant reflector are linked together in the fitting. The letter "$p$" is included in confidence limits that have pegged at a limiting value allowed in the model.
[a] Cross-normalizations are relative to XIS-FI.
[b] The model-calculated 2–10 keV flux is quoted for XIS-FI.

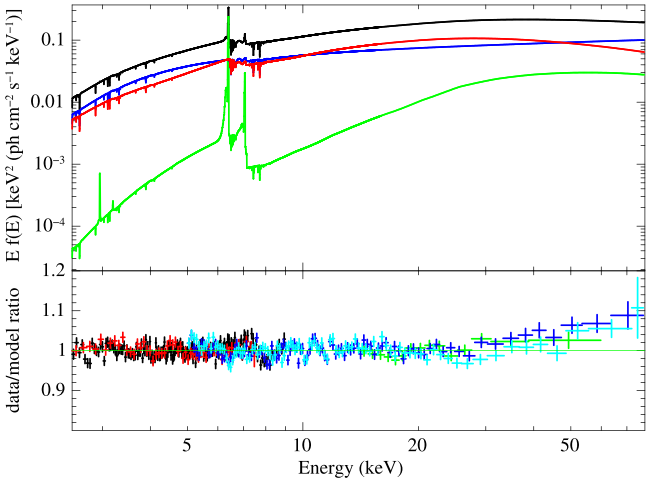


**Figure 5.** Top panel: model plotted in $Ef(E)$. The components are, from top to bottom, the total model (black), the cut-off power law (dark blue), the inner disk reflection component (red), and the distant reflector component (green). Bottom panel: the data/model ratios for XIS-FI (black), XIS-1 (red), PIN (green), FPMA (dark blue), and FPMB (light blue). The green line indicates a data/model ratio of unity. For plotting purposes only, spectral bins have either a significance of $80\sigma$ or a maximum of 80 spectral channels.

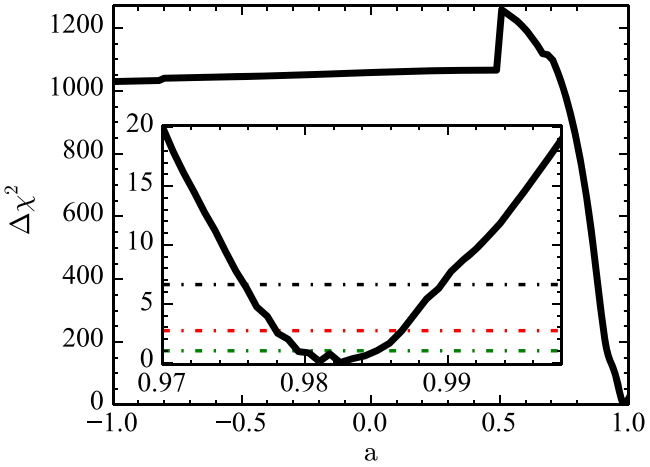


**Figure 6.** $\Delta\chi^2$ vs. the dimensionless spin parameter illustrating our statistical spin constraint. The inset shows the range $a > 0.97$. 68%, 90%, and 99% confidence levels for one interesting parameter are indicated with dashed lines, which correspond to $\Delta\chi^2$ values of 1.00, 2.71, and 6.63, respectively.

this to limit the influence of the degeneracy between the black hole spin and the Fe abundance (Reynolds et al. 2012). As shown in Table 2, the inclusion of the IDR is motivated by a reduction in $\chi^2/\nu$ by $\Delta\chi^2/\Delta\nu = -1060/-7$.

In summary, our model has the functional form `(Tbabs)*((partcov*zTbabs)*WA1*WA2*(xillver + highecut*zpowerlw + relconv*xillver))`. Best-fit parameter values are shown in Table 3, and the best-fit model and data/model ratios are shown in Figure 5.

Applying an IDR model, we find strong evidence for relativistic reflection and a preliminary SMBH spin constraint $a = 0.98 \pm 0.01$ as shown in Figure 6. If we calculate the reflection fraction, $R$, as the ratio of the inner disk reflector flux to the PLC flux in the 20–40 keV band, we find that $R = 1.3 \pm 0.2$. This reflection fraction is relatively low given the near-maximal spin and relatively steep inner emissivity index, $q_1 = 10.0^{+0.0p}_{-0.4}$, with respect to the maximum expected reflection fraction in the lamp post geometry (Dauser et al. 2014). We discuss this further in Section 5.

We find a partial-covering fraction that is consistent with a scattered fraction. Parameters largely do not show degeneracies as illustrated with confidence intervals in Figure 7. We do find a degeneracy between the inner disk component spin and inclination although we find values for these parameters that are consistent with previous studies as discussed in Section 5. For the cut-off PLC, we find only a lower limit $E_{\rm cut} > 600$ keV if we allow the cut-off energy to fit freely. For simplicity, we fix $E_{\rm cut} = 1000$ keV in the best-fit model and find $\Gamma = 1.75^{+0.01}_{-0.02}$.

To illustrate the spectral features that are modeled by the IDR, we remove this component from the best-fit model giving the data/model ratios shown in Figure 8. We then refit this model, which gives a significantly worse fit than the best-fit model ($\Delta\chi^2/\Delta\nu = +1060/+7$). This increase in $\chi^2$ is driven by residuals in the Fe K-band and the energy range $E \gtrsim 10$ keV identical to those motivating its inclusion.

We note that non-unity ratios remain at the <10% level in the best-fit data/model ratios at energies $E \gtrsim 30$ keV, as $\chi^2/\nu = 1304/1219$ (1.07) ignoring data below 30 keV. We attempt to account for these non-unity ratios with a phenomenological hard PLC, which have been observed in radio-loud AGNs (e.g., 3 C 273; Grandi & Palumbo 2004), in order to test whether this may be emission from the dim, extended radio jet in the source (Mundell et al. 2003; Wang et al. 2011a). The hard PLC fits with $\Gamma_{\rm hard} = 1.23^{+0.05}_{-0.10}$, and the coronal power law $\Gamma$ increases to $\Gamma = 1.83^{+0.03}_{-0.02}$. This component gives a small but significant reduction in the fit statistic of $\Delta\chi^2/\Delta\nu = -39/-2$. The presence of such a hard PLC, which could perhaps correspond to extended jet emission, would be interesting although we caution that the component is mainly significant in an energy band where there is more uncertainty in the *NuSTAR* calibration.

In an attempt to constrain the outer extent of the corona, we try replacing the `relconv` component in the best-fit model with a relativistic convolution component with a twice broken power-law emissivity profile, `kdblur3` (Wilkins & Fabian 2011). We allow the inner disk radius to fit freely because the spin is fixed at $a = 0.998$. The outer index is fixed to $q_3 = 3$ as expected from basic geometry at radii in the disk where $r \gg h$. We limit the outer break radius to values $r_{\rm br,2} > 10\ r_g$, and we find $r_{\rm br,2} = 10^{+6}_{-0p}\ r_g$. We also find $r_{\rm in} = 1.5 \pm 0.1\ r_g$, $q_1 = 10.0^{+0.0p}_{-0.4}$, $r_{\rm br,1} = 3.5 \pm 0.1\ r_g$, and $q_2 = 2.5^{+0.3}_{-0.2}$. This model provides only a slightly better fit than the best-fit model ($\Delta\chi^2/\Delta\nu = -4/-1$), so a twice-broken power-law emissivity profile is not strongly warranted statistically.

If we apply a lamp post model, `relconv_lp` (Dauser et al. 2013), in place of `relconv` in the best-fit model, we find a lamp post height $h = 1.3^{+0.1}_{-0.0p}\ r_g$ and a reflection fraction consistent with the best-fit model ($R = 1.2 \pm 0.1$) although we also find a significantly worse fit ($\Delta\chi^2/\Delta\nu = +493/+2$ relative to the best-fit model). We note that the worse fit with `relconv_lp` results from the inner disk emissivity profile being determined solely with the lamp post height compared to the broken power-law profile used in `relconv`.

We attempt to add a second lamp post component by including a second inner disk component because coronae could be extended, such as in a scenario where a jet produces

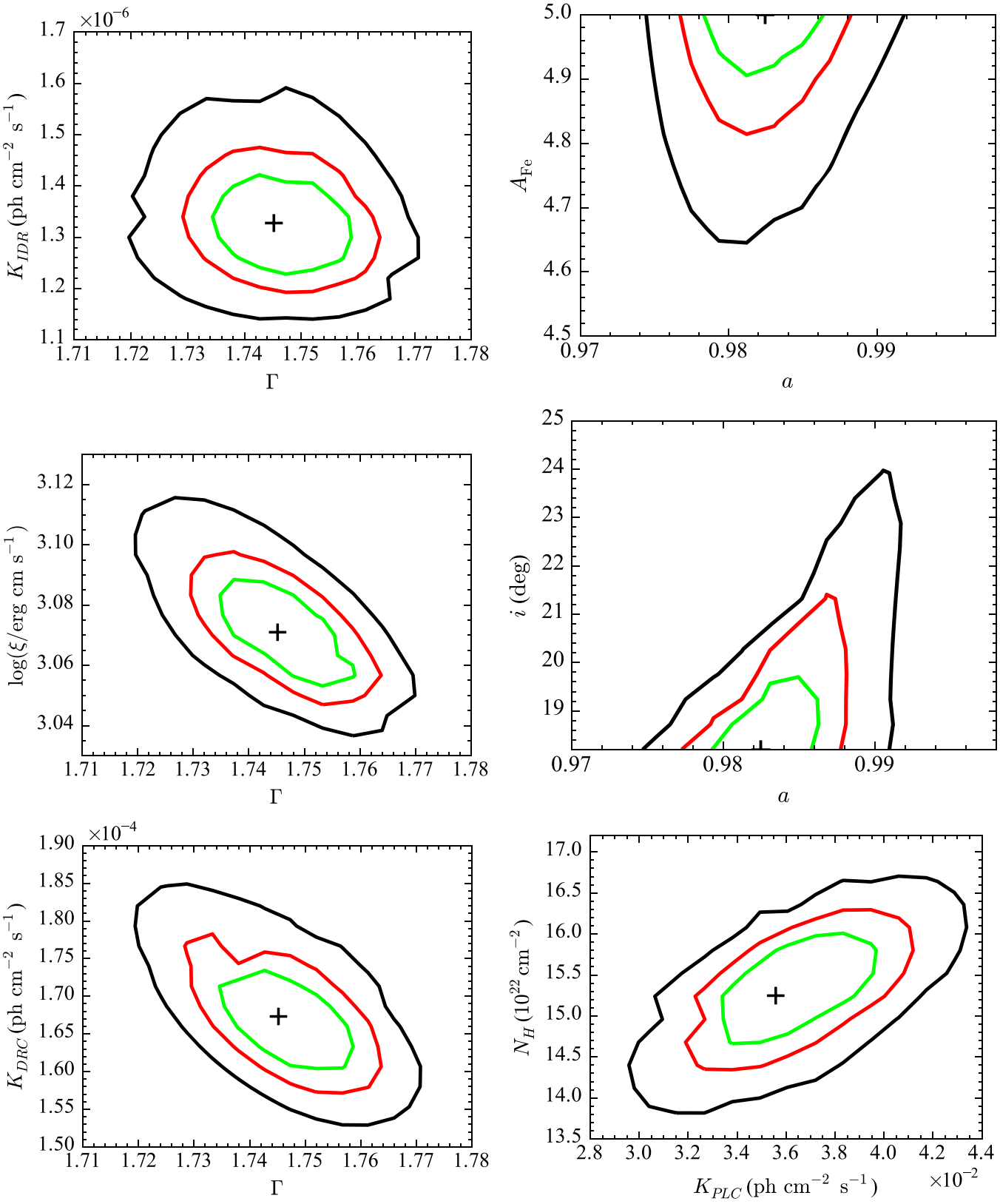


**Figure 7.** Confidence contours for the inner disk reflection time-averaged model. Confidence contours indicate 99% (black), 90% (red), and 68% (green) confidence intervals in two interesting parameters, which correspond to $\Delta\chi^2$ values of 9.21, 4.61, and 2.30, respectively. Confidence contours are shown for the plane of the PLC $\Gamma$ and the IDR normalization (top left), the plane of $a$ and $A_{\rm Fe}$ (top right), the plane of the PLC $\Gamma$ and the IDR $\xi$ (middle left), the plane of the IDR $a$ and inclination (middle right), the plane of the PLC $\Gamma$ and the distant reflector normalization (bottom left), and the plane of the PLC normalization and the partial covering absorber $N_{\rm H}$ (bottom right).

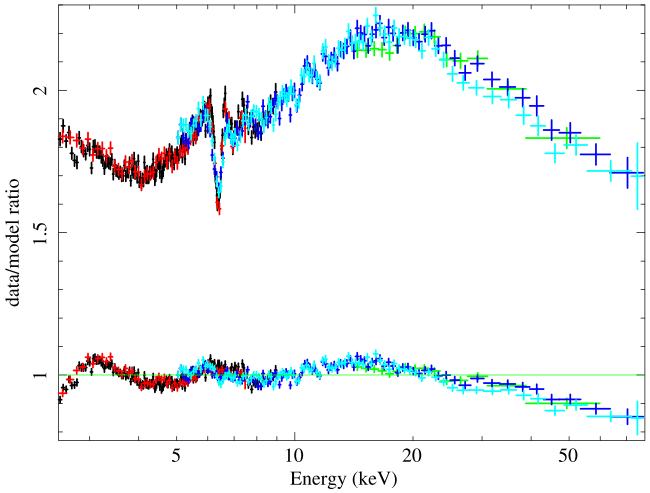


**Figure 8.** Data/model ratios are shown after starting with the best-fit model and then removing the inner disk reflection component without refitting (ratios at top) to illustrate the spectral features this component accounts for. Best-fit ratios after refitting with $\Gamma = 1.75$ fixed are shown on the bottom. Spectra are rebinned strictly for plotting purposes to have bins either with a significance of $80\sigma$ or a maximum of 80 spectral channels. Also, the green line indicates a data/model ratio of unity.

the coronal emission or a corona has multi-site activity. We fix all of its parameters to those of the first inner disk component except for the normalization and lamp post height. We find a similar reflection fraction and an improved fit relative to the single lamp post model ($\Delta\chi^2/\Delta\nu = -240/-2$) where the second lamp post component has height $h = 17 \pm 3\ r_g$ and low flux relative to the first lamp post component, which again fits with a low height $h = 1.3^{+0.3}_{-0.0p}\ r_g$. This fit along with our best-fit model indicate that a model more complicated than a single point source on the spin axis provides a statistically favored description of the reflection spectrum. This fit also suggests that the corona may have an extended component.

In attempt to test the extended corona scenario self-consistently, we apply the `relconv_LP_ext` model (Dauser et al. 2013). We model the disk-illuminating source as an outflow on the spin axis with outflow velocity $v_{\rm out}$, base height $h_{\rm base}$, and maximum height $h_{\rm top}$. We fix $h_{\rm base}$ to the event horizon radius as motivated by the dual lamp post model described above. We find $v_{\rm out}/c = 0.01^{+0.08}_{-0.01p}$ and $h_{\rm top} = 1.3^{+0.1}_{-0.0p}\ r_g$. This model (which gives $\Delta\chi^2/\Delta\nu = +477/+1$ relative to the best-fit model) is consistent with the single lamp post model presented above within errors. We find a better fit with the dual lamp post model than with this extended corona model, which may result from describing the corona with two physically discrete illuminating components rather than a continuous illuminating source.

We try applying the `relxill` model in place of the IDR component in the best-fit model to more accurately account for the emission angle as a function of radius. The IDR models we employ in the best-fit model assume a single emission angle for the inner accretion disk emission and also assume an isotropic emission distribution. While these are valid assumptions for constraining properties of relativistic reflection, the emission angle of photons leaving the disk is not constant and depends upon radius, especially in the innermost regions of the disk as a consequence of relativistic light-bending (García et al. 2014).

**Table 4**
Absorption-dominated Model Time-averaged Best-fit Values

| Component | Parameter (Units) | Value |
|---|---|---|
| PC1 | $N_{\rm H}$ ($\rm cm^{-2}$) | $(13.3 \pm 0.9) \times 10^{22}$ |
| | $f_{\rm cov}$ | $0.94 \pm 0.01$ |
| PC2 | $N_{\rm H}$ ($\rm cm^{-2}$) | $56^{+3}_{-4} \times 10^{22}$ |
| | $f_{\rm cov}$ | $0.42 \pm 0.02$ |
| Warm absorber 1 | $N_{\rm H}$ ($\rm cm^{-2}$) | $1.6^{+0.5}_{-0.3} \times 10^{22}$ |
| | $\log(\xi/\ {\rm erg\ cm\ s^{-1}})$ | $2.52^{+0.07}_{-0.02p}$ |
| Warm absorber 2 | $N_{\rm H}$ ($\rm cm^{-2}$) | $5.9^{+0.5}_{-0.4} \times 10^{22}$ |
| | $\log(\xi/\ {\rm erg\ cm\ s^{-1}})$ | $3.46 \pm 0.03$ |
| DRC | $A_{\rm Fe}$ | $1.5^{+0.2}_{-0.1}$ |
| | $K_{\rm DRC}$ (ph $\rm cm^{-2}\ s^{-1}$) | $(4.3 \pm 0.2) \times 10^{-4}$ |
| | $\log(\xi/\ {\rm erg\ cm\ s^{-1}})$ | 0 ($f$) |
| PLC | $\Gamma$ | $1.92 \pm 0.01$ |
| | $E_{\rm cut}$(keV) | 1000($f$) |
| | $K_{\rm PLC}$ (ph $\rm cm^{-2}\ s^{-1}$) | $0.117^{+0.002}_{-0.003}$ |
| Fit | $\chi^2/\nu$ | 4539/4106 (1.11) |

**Note.** Statistical errors are quoted to the 90% confidence level. Instrument cross-normalizations and model-predicted fluxes are consistent with those shown in Table 3. The redshifts of all components of the source are fixed to the systemic value, $z = 0.00332$. PC1 and PC2 indicate partial-covering absorbers 1 and 2, DRC indicates distant reflection component, and PLC indicates power-law component.

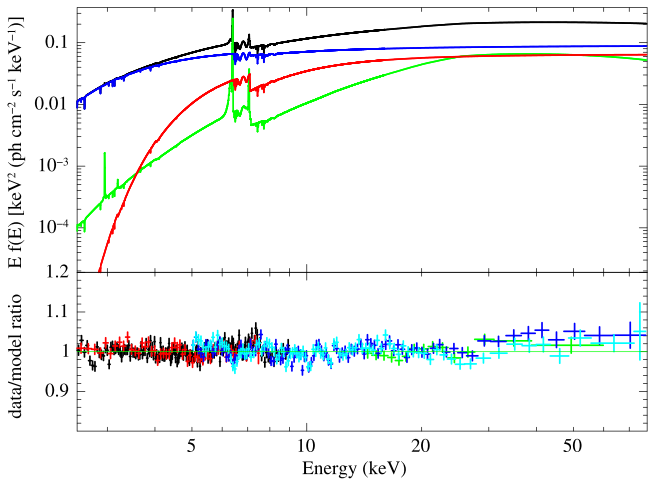


**Figure 9.** Top panel: absorption-dominated model plotted in $Ef(E)$. The broadband components are, from top to bottom, the total model (black), the coronal power-law component that is absorbed by PC2 (red), the power-law component that is not absorbed by PC2 (blue), and the distant reflector component (green). Bottom panel: the data/model ratios for XIS-FI (black), XIS-1 (red), PIN (green), FPMA (dark blue), and FPMB (light blue). The green line indicates a data/model ratio of unity. For plotting purposes only, spectral bins have either a significance of $80\sigma$ or a maximum of 80 spectral channels.

We find parameter values consistent within errors with those for the best-fit model including a reflection fraction in the 20–40 keV band $R = 1.3 \pm 0.2$ and a similar fit to the best-fit model ($\Delta\chi^2/\Delta\nu = -5/+0$). Consequently, the assumption of a single emission angle for the inner accretion disk does not introduce significant systematic error into our results.

**Table 5**
Exposure Times and Background Subtracted Counts for the *Suzaku* and *NuSTAR* Time-resolved Data

| | XIS-FI | | XIS-1 | FPMA | | FPMB |
|---|---|---|---|---|---|---|
| Int. | Time(s) | Counts | Counts | Time(s) | Counts | Counts |
| 1 | 2776 | 18211 | 7245 | 2959 | 13225 | 12946 |
| 2 | 19535 | 137709 | 55138 | 18680 | 98549 | 90109 |
| 3 | 6920 | 40678 | 15810 | 6319 | 31340 | 30462 |
| 4 | 24474 | 127483 | 49964 | 23550 | 108053 | 103254 |
| 5 | 7640 | 48024 | 18871 | 7318 | 39132 | 37702 |
| 6 | 2423 | 17205 | 7043 | 2906 | 16372 | 15494 |
| 7 | 6055 | 35980 | 14411 | 7120 | 34199 | 32830 |

**Note.** Counts correspond to the 2.5–9 keV energy bandpass for XIS-FI, 2.5–7.5 keV for XIS-1, and 5–79 keV for FPMA and FPMB. The relatively low exposure times for the interval six data result from relatively poor overlap between the *NuSTAR* and *Suzaku* observations during this interval.

#### 4.1.2. Absorption-dominated Model

We investigate an absorption-dominated model and develop a model that has the functional form `(Tbabs) * (WA1 * WA2 * (partcov* zTbabs) * (partcov* zTbabs) * (xillver + zpowerlw))`. We find a best-fit model shown in Table 4 and Figure 9. This model provides a statistically less satisfactory description of the time-averaged data ($\Delta\chi^2/\Delta\nu = +86/+5$) relative to the best-fit model.

The absorption-dominated model also has positive residuals at the <10% level at energies $E > 30$ keV, so we also attempt adding a hard PLC to it. We find a similar hard PLC as for the IDR model with $\Gamma_{\rm hard} = 1.25^{+0.08}_{-0.07}$ can account for the high energy non-unity ratios. We also find a moderate reduction in the fit statistic of $\Delta\chi^2/\Delta\nu = -24/-2$.

### 4.2. Time-resolved Analysis

To perform the time-resolved analysis, we produce strictly simultaneous time-resolved data products (i.e., the data products are time-filtered to only include times when the two observatories were simultaneously viewing NGC 4151) in seven time-intervals as shown in Figure 2. Intervals are chosen to maximize S/N and have approximately constant HRs. We omit making PIN time-resolved products due to *NuSTAR*'s superior sensitivity at $E > 10$ keV. Information for the time-resolved data is shown in Table 5. We note that similar time-resolved analyses have been performed on joint *NuSTAR* observations with *Suzaku* or *XMM-Newton* of the Seyfert galaxies IC 4329 A (Brenneman et al. 2014), NGC 1365 (Walton et al. 2014), and MCG 6-30-15 (Marinucci et al. 2014b).

To first assess the spectral variability in a model independent fashion, we analyze difference spectra between high flux states (intervals 2 and 6) and a low flux state (interval 4) as shown in Figure 10. The difference spectra peak at $E \sim 3$ keV and gradually decrease with increasing energy. Additionally, the flux of the narrow, neutral Fe K$\alpha$ line at 6.4 keV varies less than the continuum.

To fully assess the spectral variability, we perform a joint fit of the time-resolved spectra using a strategy similar to our time-averaged analysis. We initially set the parameter values to their time-averaged model values (which are shown in Tables 3 and 4). We require many parameters to fit freely to the same value across all intervals on physical grounds. We assume the instrument cross-normalizations are constant during the observations. The DRC, which likely arises from material at distances in the range $r \sim 7$ lt-day (which corresponds to the approximate distance to the optical broad-line region in the source; Bentz et al. 2006) to $r \sim 4.2 \times 10^4$ lt-day (which is the upper limit on the size of a dusty torus in the source; Radomski et al. 2003), likely does not vary on the time-scale of the observations as also suggested by the rms $F_{\rm var}$ of the data. The Fe abundance and inclination of the inner accretion disk also can be assumed to be constant during the observations. Similarly, the black hole spin can be safely assumed to be constant, as SMBH angular momentum evolves only on cosmic timescales from accretion and/or mergers (e.g., Berti & Volonteri 2008). We additionally fix the WA2 ionization parameter to its time-averaged best-fit value.

#### 4.2.1. IDR Model

We systematically assess which parameters should be variable and constant in the time-resolved analysis by carrying out fits for all combinations of variable parameters for the following seven parameters: neutral absorber $N_{\rm H}$, $f_{\rm cov}$, DRC normalization ($K_{\rm DRC}$), PLC $\Gamma$, PLC 20–40 keV flux ($F_{\rm PLC}$), IDR $\xi$, and IDR 20–40 keV flux ($F_{\rm IDR}$). We parameterize the normalizations of the PLC and IDR in terms of their 20–40 keV flux for the time-resolved analysis using the `cflux` model in `XSPEC`. We allow parameters to be variable until we no longer find an improvement in the fit based on the F-test. We find a best-fit time-resolved fit with four variable parameters ($F_{\rm PLC}$, $F_{\rm IDR}$, $N_{\rm H}$, and $\Gamma$). If we additionally try allowing $f_{\rm cov}$ to be variable, it provides a marginally significant improvement to the fit according to the F-test ($\Delta\chi^2/\Delta\nu = -30/-6$). We find that this parameter is correlated with the power-law normalization, which is likely unphysical whether the covering fraction represents a scattered fraction or a true covering fraction for a neutral absorber. Thus, we elect to keep the covering fraction constant.

In summary, the best-fit time-resolved model values are shown in Tables 6 and 7. Time-series of the parameter values allowed to vary between intervals (see Figure 11) show that modest coronal and IDR flux variation drives the spectral variability during the observations. Note the similarity of the variation in the PLC 20–40 keV flux and the 30–79 keV flux shown in Figure 2. The reflection fraction (i.e., the ratio of the IDR and the PLC 20–40 keV fluxes) is anti-correlated with the PLC 20–40 keV flux. This anti-correlation is reasonable with respect to some of the predictions of the lamp post model for a near-maximal, prograde black hole spin. Specifically, for small lamp post heights, the reflection fraction can increase when the lamp post moves to smaller heights due to a decrease in the continuum flux that reaches the observer (Miniutti & Fabian 2004; Dauser et al. 2014).

#### 4.2.2. Absorption-dominated Model

For the absorption-dominated model, we carry out a similar systematic analysis as followed for the IDR model. We perform fits for all combinations of variable parameters for the following seven parameters: the column densities and covering fractions of both neutral absorbers, DRC normalization ($K_{\rm DRC}$), PLC $\Gamma$, and the PLC 20–40 keV flux ($F_{\rm PLC}$). We allow parameters to be variable until we no longer find an improvement in the fit based on the F-test. We find a best-fit

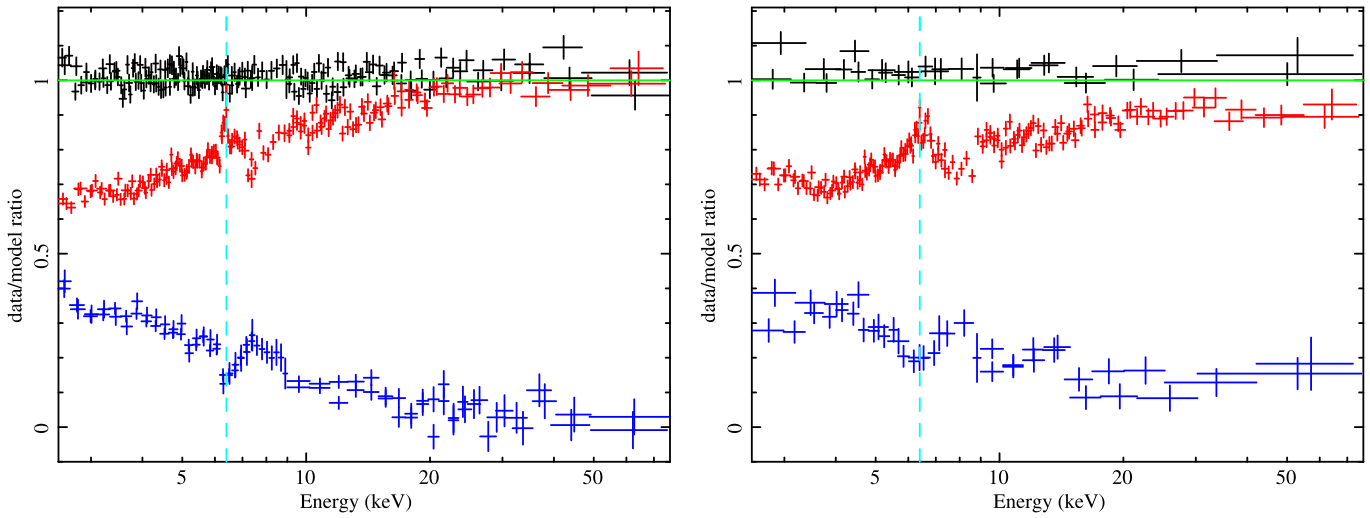


**Figure 10.** Left: the ratios of the interval 2 (black, top), interval 4 (red, middle), and difference (blue, bottom) spectra to the best-fit model to interval 2. Right: the ratios of the interval 6 (black, top), interval 4 (red, middle), and difference (blue, bottom) spectra to the best-fit model to interval 6. Notice the narrow dip in both difference spectra at the energy of neutral Fe K$\alpha$ (6.4 keV as indicated with a dashed, light blue line). XIS-FI, XIS-1, FPMA, and FPMB spectra are shown although only *NuSTAR* data is shown above 9 keV and only *Suzaku* data is below 9 keV for clarity. Spectra have been rebinned for plotting purposes only. The solid green line indicates a data/model ratio of unity.

**Table 6**
Time-resolved Best-fit Values for Parameters Free to Fit within Each Interval for the Inner Disk Reflection Model

| Int. | $N_{\rm H}$ ($10^{22}$ cm$^{-2}$) | log(F$_{\rm PLC}$/ erg cm$^{-2}$ s$^{-1}$ ) | $\Gamma$ | log(F$_{\rm IDR}$/ erg cm$^{-2}$ s$^{-1}$ ) |
|---|---|---|---|---|
| 1 | $14.1^{+0.8}_{-1.0}$ | $-9.97^{+0.07}_{-0.09}$ | $1.78 \pm 0.04$ | $-10.14^{+0.10}_{-0.14}$ |
| 2 | $13.8^{+0.6}_{-0.8}$ | $-9.96 \pm 0.04$ | $1.77 \pm 0.02$ | $-10.02^{+0.05}_{-0.04}$ |
| 3 | $15.0^{+1.0}_{-1.2}$ | $-10.12^{+0.08}_{-0.05}$ | $1.73 \pm 0.03$ | $-9.88 \pm 0.05$ |
| 4 | $15.7^{+1.1}_{-1.5}$ | $-10.22^{+0.07}_{-0.11}$ | $1.73 \pm 0.03$ | $-9.86 \pm 0.04$ |
| 5 | $16.9^{+0.9}_{-1.3}$ | $-9.93^{+0.05}_{-0.07}$ | $1.72^{+0.03}_{-0.02}$ | $-9.98^{+0.06}_{-0.07}$ |
| 6 | $15.0^{+0.9}_{-1.0}$ | $-9.85^{+0.07}_{-0.08}$ | $1.73^{+0.03}_{-0.04}$ | $-10.08^{+0.11}_{-0.12}$ |
| 7 | $14.2^{+0.9}_{-1.1}$ | $-10.05^{+0.06}_{-0.08}$ | $1.74^{+0.02}_{-0.04}$ | $-9.96^{+0.05}_{-0.06}$ |
| Fit | $\chi^2/\nu$ | 15655/15589(1.00) | … | … |

**Note.** 90% confidence intervals are given for the variable parameters for the inner disk reflection model, which are the partial covering absorber column density, power-law component flux in the 20–40 keV band, power-law component photon index, and IDR 20–40 keV flux.

**Table 7**
Time-resolved Best-fit Values for Inner Disk Reflection Model Parameters Assumed to Not Vary During the Observations

| Comp. | Par. (Units) | Values |
|---|---|---|
| PC1 | $f_{\rm cov}$ | $0.93 \pm 0.01$ |
| WA1 | $N_{\rm H}$ (cm$^{-2}$ ) | $2.9^{+1.0}_{-0.7} \times 10^{22}$ |
| | log($\xi$/ erg cm s$^{-1}$) | 2.5($f$) |
| WA2 | $N_{\rm H}$ (cm$^{-2}$ ) | $(2.2 \pm 0.9) \times 10^{22}$ |
| | log($\xi$/ erg cm s$^{-1}$) | $3.4^{+0.2}_{-0.1}$ |
| DRC | $A_{\rm Fe}$[a] | $5.0^{+0.0p}_{-0.3}$ |
| | $K_{\rm DRC}$ (ph cm$^{-2}$ s$^{-1}$ ) | $(1.6 \pm 0.2) \times 10^{-4}$ |
| IDR | $q_1$ | $10.0^{+0.0p}_{-0.6}$ |
| | $q_2$ | $2.8^{+0.2}_{-0.1}$ |
| | $r_{\rm br}$ ( $r_g$) | $3.3^{+0.2}_{-0.1}$ |
| | $a$ | $0.98 \pm 0.01$ |
| | log($\xi$/ erg cm s$^{-1}$) | $3.06^{+0.02}_{-0.03}$ |
| | $i$ (degree) | $18^{+5}_{-0p}$ |
| Cross-norm.[b] | XIS-1 | $0.95 \pm 0.01$ |
| | FPMA | $1.03^{+0.01}_{-0.01}$ |
| | FPMB | $1.07^{+0.01}_{-0.01}$ |
| Fit | $\chi^2/\nu$ | 15655/15589(1.00) |

**Notes.** 90% confidence intervals are given. WA1 and WA2 indicate warm absorbers one and two, respectively, PC1 indicates the partial covering, neutral absorber, DRC indicates the distant reflection component, PLC indicates the power-law component, and IDR indicates the inner disk reflection component.
[a] The Fe abundances of the IDR and DRC components are linked together in the fitting.
[b] Cross-normalizations are relative to XIS-FI.

time-resolved fit with four variable parameters ($F_{\rm PLC}$, $\Gamma$, and $N_{\rm H}$ and $f_{\rm cov}$ of PC2) as shown in Figure 12. For the time-resolved analysis, we allow these four parameters to fit independently in each interval (which are shown in Table 8) and allow all other free parameters (which are shown in Table 9) to fit freely but linked between each interval.

We find a best-fit absorption-dominated model that provides a slightly worse fit of the time-resolved data ($\Delta\chi^2/\Delta\nu = +29/+5$) relative to the IDR model. Within the context of the absorption-dominated model, variation in the covering fraction of PC2 and the PLC flux drives the variability during the observations. The PC2 $N_{\rm H}$ and $f_{\rm cov}$ parameters appear to be correlated with variations in the coronal continuum on the short timescales seen in the top panel of Figure 12. We show correlation plots in the bottom panel of Figure 12 to show that $f_{\rm cov}$ and $F_{\rm PLC}$ have closed confidence contours.

## 5. DISCUSSION

Using timing and spectral analyses, we have characterized the constant and variable spectral behavior of NGC 4151 as observed simultaneously with *NuSTAR* and *Suzaku*. Through a spectral analysis, we apply inner accretion disk reflection and

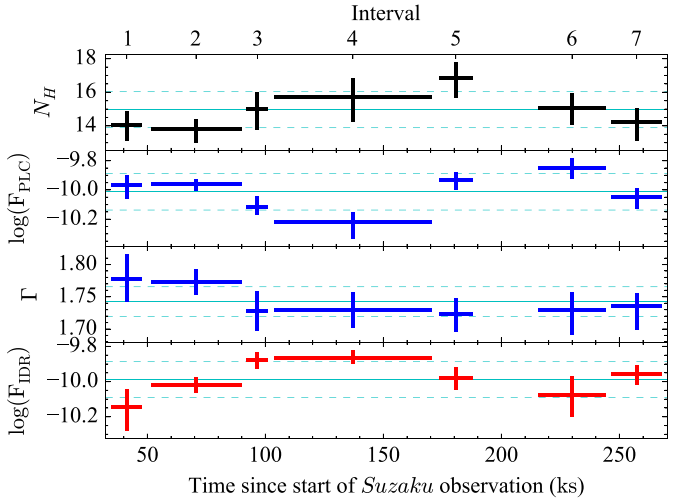


**Figure 11.** Time-resolved analysis best-fit values for the inner disk reflection model for the variable parameters, which are the partial covering absorber column density, power-law component flux in the 20–40 keV band, power-law component photon index, and IDR 20–40 keV flux. Vertical error bars indicate 90% confidence intervals, and horizontal error bars indicate the duration of the interval. Horizontal lines indicate the mean (solid) and one standard deviation (dashed).

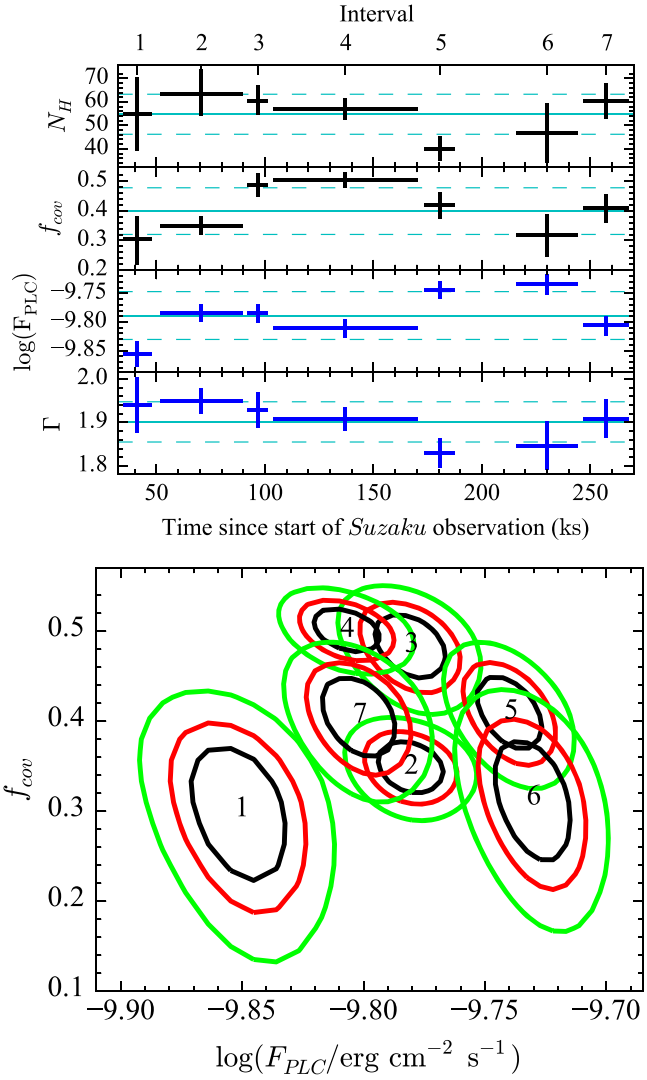


**Figure 12.** Top: best-fit values for the time-resolved analysis for the variable parameters for the absorption-dominated model, which are the PC2 covering fraction, PC2 column density, power-law component flux in the 20–40 keV band, and power-law component photon index. Vertical error bars indicate 90% confidence intervals, and horizontal error bars indicate the duration of the interval. Horizontal lines indicate the mean (solid) and one standard deviation (dashed). Bottom: absorption-dominated model confidence contours for the partial covering absorber covering fraction versus the cut-off power-law flux for the time-resolved analysis for each time interval as labeled. Confidence contours indicate 99% (green), 90% (red), and 68% (black) confidence intervals for two interesting parameters.

absorption-dominated models. We find that the IDR model provides a better fit to the time-averaged and time-resolved spectra. Within the context of the IDR model, we find evidence for relativistic reflection from the inner accretion disk and a preliminary spin measurement for the SMBH.

It is unlikely that a putative neutral absorber (which are at radii of $r \sim 10^4 - 10^5\ r_g$; Antonucci 1993; Urry & Padovani 1995) can partially cover AGN coronae (which have been found to have size $D \lesssim 10\ r_g$ for several AGNs including NGC 4151; Reis & Miller 2013). Furthermore, there is no physical reason to expect a neutral absorber to be correlated with variations in the coronal continuum on the short timescales seen in Section 4.2.2 because the neutral absorbing gas likely is located relatively far from the continuum source. A reasonable range of distances for the absorbing material might extend as close as the broad-line region ($r = 6.6^{+1.1}_{-0.8}$ lt-day; Bentz et al. 2006) and as far as the upper limit on the size of a dusty torus in the source ($r \sim 4.2 \times 10^4$ lt-day; Radomski et al. 2003). In contrast, a correlation between the IDR and the coronal continuum is physically possible based on light crossing time arguments and has been observed. The distance between the corona and the disk inferred by Cackett et al. (2014) and the size scale of the inner disk, which are both $\lesssim 10\ r_g$, correspond to a light-travel time $\lesssim 2$ ks assuming the black hole mass $M = 4.57^{+0.57}_{-0.47} \times 10^7\ M_\odot$(Bentz et al. 2006). The reverberation analysis of Zoghbi et al. (2012) shows that the IDR flux can lag behind the coronal flux on timescales ~2 ks.

Thus, on statistical and physical grounds, we discuss only the IDR model. Here, we discuss assumptions that may introduce systematic errors in the preliminary black hole spin value and physical scenarios for the disk–corona system. For calculations that use the black hole mass, we use $M = 4.57^{+0.57}_{-0.47} \times 10^7\ M_\odot$ (Bentz et al. 2006) measured from optical and UV reverberation.

### 5.1. Systematic Uncertainties in the Black Hole Spin

Assumptions in our model introduce systematic uncertainty into the derived confidence intervals in the dimensionless black hole spin. A primary assumption of modeling the IDR with the `relconv` kernel is that the accretion disk is radiatively efficient, optically thick, and geometrically thin at radii greater than or equal to the ISCO radius. These assumptions generally should be applicable to NGC 4151 considering the modest accretion rate implied by its bolometric luminosity $L_{\rm bol} \sim 0.01 L_{\rm Edd}$. The assumption of a geometrically thin disk breaks down where the disk thickness, $t$, is on the same order as the radius in the disk, $r$, or $t/r \sim 1$. For Seyfert galaxies with Eddington ratios in the range $L_{\rm bol}/L_{\rm Edd} \sim 0.01{-}0.3$, we expect disk thicknesses in the range $t \sim (0.1 - 1.0)\ r_g$ for a Shakura & Sunyaev (1973) disk. Thus, this assumption may be invalid for $r_{\rm in} \lesssim 2\ r_g$, which corresponds to spins $a \gtrsim 0.94$. Thus, considering the finite thickness of the disk close to the black

**Table 8**
Time-resolved Best-fit Values for Parameters Free to Fit within Each Interval for the Absorption-dominated Model

| Int. | $f_{cov}$ | $N_H$ ($10^{22}$ cm$^{-2}$) | $\log(F_{PLC}/$ erg cm$^{-2}$ s$^{-1}$) | $\Gamma$ |
|---|---|---|---|---|
| 1 | $0.30 \pm 0.08$ | $55 \pm 16$ | $-9.86^{+0.03}_{-0.02}$ | $1.94^{+0.07}_{-0.06}$ |
| 2 | $0.35 \pm 0.03$ | $64 \pm 10$ | $-9.78^{+0.01}_{-0.02}$ | $1.95 \pm 0.03$ |
| 3 | $0.49^{+0.03}_{-0.04}$ | $61^{+6}_{-7}$ | $-9.78^{+0.01}_{-0.02}$ | $1.93 \pm 0.04$ |
| 4 | $0.51^{+0.02}_{-0.03}$ | $57^{+5}_{-4}$ | $-9.81^{+0.01}_{-0.02}$ | $1.91^{+0.02}_{-0.03}$ |
| 5 | $0.42^{+0.04}_{-0.05}$ | $40 \pm 5$ | $-9.74^{+0.01}_{-0.02}$ | $1.83 \pm 0.03$ |
| 6 | $0.32^{+0.07}_{-0.08}$ | $47 \pm 13$ | $-9.73^{+0.01}_{-0.02}$ | $1.85^{+0.05}_{-0.06}$ |
| 7 | $0.41 \pm 0.05$ | $61^{+7}_{-8}$ | $-9.81^{+0.02}_{-0.01}$ | $1.91 \pm 0.04$ |
| Fit | $\chi^2/\nu$ | 15684/15594(1.01) | … | … |

**Note.** 90% confidence intervals are given for the variable parameters for the absorption-dominated model, which are the PC2 covering fraction, PC2 column density, power-law component flux in the 20–40 keV band, and power-law component photon index.

**Table 9**
Time-resolved Best-fit Values for Parameters Assumed to not Vary During the Observations for the Absorption-dominated Model

| Comp. | Par. (Units) | Values |
|---|---|---|
| PC1 | $N_H$ (cm$^{-2}$) | $13.5^{+0.9}_{-1.0} \times 10^{22}$ |
| | $f_{cov}$ | $0.94 \pm 0.01$ |
| WA1 | $N_H$ (cm$^{-2}$) | $(1.6 \pm 0.5) \times 10^{22}$ |
| | $\log(\xi/$ erg cm s$^{-1}$) | $2.5(f)$ |
| WA2 | $N_H$ (cm$^{-2}$) | $5.9^{+0.9}_{-0.7} \times 10^{22}$ |
| | $\log(\xi/$ erg cm s$^{-1}$) | $3.5 \pm 0.1$ |
| DRC | $A_{Fe}$[a] | $1.7^{+0.2}_{-0.3}$ |
| | $K_{DRC}$ (ph cm$^{-2}$ s$^{-1}$) | $(4.1 \pm 0.3) \times 10^{-4}$ |
| Cross-norm.[b] | XIS-1 | $0.95 \pm 0.01$ |
| | FPMA | $1.03 \pm 0.01$ |
| | FPMB | $1.06 \pm 0.01$ |
| Fit | $\chi^2/\nu$ | 15684/15594(1.01) |

**Notes.** 90% confidence intervals are given. WA1 and WA2 indicate warm absorbers one and two, respectively, PC1 indicates the partial covering, neutral absorber, DRC indicates the distant reflection component, and PLC indicates the power-law component.
[a] The Fe abundances of the IDR and DRC components are linked together in the fitting.
[b] Cross-normalizations are relative to XIS-FI.

hole, we estimate that this assumption relaxes our spin constraint to $a > 0.94$.

We assume that the inner accretion disk radius is the ISCO radius and that a negligible level of emission originates within that radius. The latter assumption is supported by the near-maximal spin and relatively low Eddington ratio of the source, which may indicate that some of the accretion flow within the ISCO radius is optically thin (Reynolds & Fabian 2008). Additionally, when we allow the inner edge of the accretion disk to fit freely, it fits to a value consistent with the ISCO radius although we restrict it to fit to values $r_{in} \geqslant r_{ISCO}$. Based on MHD simulations (Reynolds & Fabian 2008), if significant emission comes from within the ISCO radius, the fit will be biased to higher spins systematically with error $\lesssim$2% for rapidly spinning, prograde black holes ($a \geqslant 0.9$). Thus, we estimate this assumption adds $\sim$ 2% systematic uncertainty to our spin value. Including the systematic uncertainties introduced by our assumptions about the thickness and extent of the inner disk, we find a constraint $a > 0.9$.

Black hole spin has some degeneracy with the iron abundance of the inner disk, as both properties affect the strength of the broad Fe line (e.g., Reynolds et al. 2012). We find that NGC 4151 has a super-solar Fe abundance. There is no apparent degeneracy between our derived Fe abundance and spin values as shown in Figure 7. Fe abundance is constant on long timescales. There is evidence for super-solar Fe abundance in material distant from the SMBH. From several *Ginga* measurements, Yaqoob et al. (1993) report an average value $A_{Fe} \sim 2.5$ from modeling an Fe K absorption edge. From analyzing the strength of a neutral Fe absorption edge in *XMM-Newton* observations, Schurch et al. (2003) report an Fe abundance $A_{Fe} \sim 3.6$, and they report $A_{Fe} \sim 2.0$ if they associate the Fe abundance of the neutral absorber with that of a Compton reflection component.

For the Fe abundance of the inner disk, Nandra et al. (2007) measure an Fe abundance in the range $A_{Fe} = 0.3$–$0.5$ from analyzing three *XMM-Newton* observations. They assume the DRC and IDR component (which are modeled with `pexmon` and `kdblur2*pexmon`, respectively) are chemically homogeneous in the same way as in the present work. Nandra et al. (2007) caution that their *XMM-Newton* values require high sensitivity, broadband observations that can simultaneously constrain the Fe K$\alpha$ line and Compton hump reflection features. Our analysis simultaneously constrains both features, and our derived Fe abundance ($A_{Fe} = 5.0^{+0.0p}_{-0.1}$) is moderately high in comparison with measurements of super-solar Fe abundance in material distant from the SMBH. This may introduce some bias into our spin constraint as a result of the positive correlation between spin and the Fe abundance (Reynolds et al. 2012). However, we conclude that our derived Fe abundance negligibly biases our spin constraint of $a > 0.9$.

Black hole spin can show a degeneracy with the disk inclination if the blue wing of the broad Fe line profile is not significantly detected, as both parameters affect the width of the broad Fe line profile. A degeneracy is seen between the disk inclination and spin shown in Figure 7. The inclination of the inner disk should be constant on long timescales, so we compare our determined inclination angle with various inclination angles previously reported for the source.

The inner disk inclination angle we find is consistent with most values determined for the inner disk. From the analysis of three *XMM-Newton* observations, Nandra et al. (2007) find an inclination of the inner disk of $i = 17^{+12}_{-17}$°, $i = 21^{+69}_{-21}$°, and $i = 33^{+1}_{-3}$°, respectively, where values are given for the best-fit `kdblur2*pexmon` model presented for each observation. From an ASCA observation, Yaqoob et al. (1995) find $i = 0^{+19}_{-0}$° using the `diskline` model (Fabian et al. 1989). Cackett et al. (2014) report $i < 30°$ for the inner disk from Fe K$\alpha$ reverberation measurements.

Comparing the inner disk inclination angle to that of more distant structures, our determined inner disk inclination angle is not consistent with the inclination of the narrow-line region, $45 \pm 5°$, as determined from *Hubble Space Telescope* observations (Das et al. 2005). This suggests that the inner disk and narrow-line region are misaligned. The inclination we find is consistent with the galactic disk inclination, $i \sim 21°$, as inferred from optical photometry (Simkin 1975) and Very Large Array observations of neutral hydrogen (Pedlar et al. 1992).

It is possible that some of the broad Fe K line profile may arise from an alternate mechanism than reflection from the inner accretion disk. For example, scattering in a Compton thick wind near the disk can produce broadened Fe line profiles (Sim et al. 2008). However, the strength of this feature significantly depends upon the outflow mass loss rate. A low mass outflow rate is expected for the low mass accretion rate of the source implied by its Eddington ratio $L_{\rm bol}/L_{\rm Edd} \sim 0.01$. Thus, we estimate that any contribution of scattering in a Compton-thick wind near the accretion disk to the broad Fe line is relatively weak compared to the broad line profile from inner accretion disk reflection.

### 5.2. Physical Scenarios for the Corona and Inner Accretion Disk

Our derived high inner disk emissivity index ($q_1 = 10.0^{+0.0p}_{-0.4}$) indicates that the corona that illuminates the inner disk is compact. The inner emissivity index and photon index, $\Gamma = 1.75^{+0.01}_{-0.02}$, together indicate a lamp post height $h < 10\ r_g$ assuming a lamp post geometry, as the maximum inner index for $\Gamma \sim 1.8$, $h = 10\ r_g$, and $a = 0.99$ is $q_1 \sim 3$ (Dauser et al. 2013). A lamp post height $h \lesssim 10\ r_g$ is expected in order to produce strong reflection features from which black hole spin can be well constrained (Dauser et al. 2013; Fabian et al. 2014). Furthermore, the high ionization parameter we find for the inner disk atmosphere is expected for a close illuminating source. We note that a high emissivity index ($q_1 \gtrsim 3$) is only physically consistent with a near-maximal black hole spin.

We calculate theoretical emissivity profiles for the lamp post model of Dauser et al. (2013) for our best-fit $\Gamma$ and $a$ values. For this calculation, we assume a minimum height in order to give a rough estimate of the highest emissivity index expected. We estimate a value of $q_1 \sim 7$ if we average the emissivity from $r_{\rm ISCO}$ to the emissivity break radius that we find for the best-fit model ($r_{\rm br}$). So, we find an inner emissivity that is steeper than expected for the lamp post model of Dauser et al. (2013). This partially illustrates why the broken power-law emissivity profile for the inner disk provides a better fit to the data than the lamp post emissivity profile. However, this estimate does not necessarily indicate that our best-fit model is unphysical.

We find a relatively low reflection fraction compared to the maximum expected reflection fraction, which is $R \sim 5-10$ for the lamp post model described in Section 4.1.1 with $a = 0.98 \pm 0.01$ and $h = 1.3^{+0.1}_{-0.0p}\ r_g$ (Dauser et al. 2014). This value is a factor ∼4−8 higher than what we find. There are several possible physical scenarios for the corona and inner accretion disk that may cause this apparent discrepancy.

If the corona results from a mildly relativistic outflow rather than a static region, then the reflection fraction is expected to be reduced because of relativistic aberration (e.g., Beloborodov 1999; Malzac et al. 2001). A photon index $\Gamma \sim 1.75$ indicates $v/c \sim 0.4$ near the base of an AGN jet and a reduction in the strength of reflection, $\Omega/2\pi$, by a factor of ∼10 using the disk inclination $i = 18°$ (Beloborodov 1999). This can help explain the apparently low reflection fraction we find. We note that very long baseline interferometry observations have shown that the radio jet in NGC 4151 has had a component with velocity $v \leqslant 0.050\ c$ at a distance $r \sim 0.16$ pc from the nucleus (Ulvestad et al. 2005). Thus, if the corona corresponds to the base of a mildly relativistic jet, then a mechanism is required to decelerate the jet to non-relativistic speeds on ∼0.1 pc scales. Also, an outflow tends to flatten the emissivity profile (Dauser et al. 2013). Keeping these facts in mind, an outflowing corona may help explain the low reflection fraction we find.

Truncation of the inner edge of the accretion disk at radius $r > r_{\rm ISCO}$ can similarly reduce the expected reflection fraction. Lubiński et al. (2010) conclude that the relatively weak strength of reflection from the disk they measure ($\Omega/2\pi \simeq 0.3$) from all *INTEGRAL* observations of NGC 4151 from 2003 January to 2009 June can be explained by an inner hot accretion flow surrounded by a cold disk truncated at $r_{\rm in} \sim 15\ r_g$ or, alternatively, a mildly relativistic coronal outflow. When we allow the inner radius of the accretion disk to fit freely using the `kdblur3` model as described previously, it fits to a value consistent with the ISCO radius of a black hole with the near-maximal, prograde spin that we find for the best-fit model. Thus, we do not find evidence for a truncated disk from spectral fitting of our observations.

Dilution of the reflection features may also reduce the measured reflection fraction. For a close disk-illuminating source suggested by the steep emissivity profile, it is plausible that the inner disk sees an intense irradiating flux and has a tenuous, hot atmosphere. This may have a density profile roughly similar to that of an accretion disk in hydrostatic equilibrium, for which an intense irradiating flux can lead to disk thermal instability (Ballantyne et al. 2001; Nayakshin & Dove 2001). This instability can produce a highly ionized "skin," which could both further broaden the disk reflection features and reduce the observed reflection fraction. Ballantyne et al. (2001) showed that simulated *RXTE* and ASCA data of hydrostatic reflection models (e.g., Ballantyne et al. 2001) fit with constant density models (Ross & Fabian 1993; Magdziarz & Zdziarski 1995) tend to fit with systematically low reflection fraction values because of dilution. Although *NuSTAR* provides superior sensitivity in the 20–40 keV energy band, where the reflection spectrum is almost completely independent of ionization parameter, our fit is biased toward best matching the spectral shape at lower energies ($E \lesssim 20$ keV), where the reflection spectrum is sensitive to the ionization parameter.

With the `xillver` models, we assume that the disk is illuminated at 45°. However, for a compact coronal geometry, the disk illumination may be incident on the disk at closer to grazing angles, especially within a few $r_g$ of the black hole (Dauser et al. 2013). In the innermost regions of the disk, this would enhance the influence of dilution and thus further reduce the reflection fraction.

In summary, both dilution from a highly ionized disk skin and a mildly relativistic outflow may contribute to the reduced reflection fraction that we find relative to predictions for the lamp post geometry. Because an outflow tends to flatten the emissivity profile, the formation of a highly ionized disk "skin" may be the dominant cause of the reduced reflection fraction. We do not find evidence for truncation of the inner accretion disk.

### 5.3. Coronal Properties

We model the coronal emission with a cut-off power law with $E_{\rm Cut} = 1000$ keV fixed and find $\Gamma = 1.75^{+0.01}_{-0.02}$. This value is consistent within $3\sigma$ with the average Seyfert photon index, $\Gamma = 1.84 \pm 0.03$, measured for 105 Seyfert galaxies with redshift $z \leqslant 0.1$ with *Bepposax* (Dadina 2008). It is relatively hard compared to the average photon index, $\Gamma = 1.93 \pm 0.01$, for 144 Seyfert galaxies in the second *INTEGRAL* AGN

catalog (Beckmann et al. 2009). The value we find agrees within $1\sigma$ with the correlation between the photon index and Eddington ratio for a sample of 69 radio-quiet AGNs out to $z \sim 2$ (Brightman et al. 2013), which gives $\Gamma = 1.63 \pm 0.16$ for $L_{\rm bol}/L_{\rm Edd} = 0.01$. We note that the significant dispersion in this correlation as well as uncertainty in estimating the Eddington ratio should be noted when applied to a single source.

The photon index we find is consistent with the range in photon index ($\Gamma \sim 1.7$–$1.86$) that Lubiński et al. (2010) measure for the source in a large range of X-ray flux states as observed with *INTEGRAL* during the period 2003 January to 2009 June. The energy cut-off we find is corroborated by the energy cut-offs found by Lubiński et al. (2010) for the source in high and medium flux states ($E_{\rm Cut} = 264^{+48}_{-26}$ keV and $E_{\rm Cut} > 1025$ keV, respectively), which serve as upper and lower bounds, respectively, to the 20−100 keV flux of the source in our data.

## 6. CONCLUSIONS

We present X-ray timing and spectral analyses of contemporaneous, 150 ks *NuSTAR* and *Suzaku* X-ray observations of the Seyfert 1.5 galaxy NGC 4151. We test separate IDR and absorption-dominated models in order to determine the properties of the innermost regions of the AGN. Our primary conclusions are enumerated below.

1. We find that the IDR model provides a better statistical and physical description of the data than the absorption-dominated model for both the time-averaged and time-resolved spectral analyses.
2. Within the context of this IDR model, we find that relativistic emission originates in a highly ionized inner accretion disk with a steep inner emissivity profile, which suggests a bright, compact inner disk-illuminating source. We find a relatively moderate reflection fraction with respect to predictions for the lamp post geometry. We find a preliminary, near-maximal black hole spin $a > 0.9$ accounting for statistical and systematic modeling errors.
3. Through a time-resolved spectral analysis, we find that modest coronal and IDR variation drive the spectral variability during the observations.
4. We discuss physical scenarios with respect to our derived inner accretion disk and coronal properties. We find that a compact coronal geometry can reproduce the observed features.

This work further displays the ability of *NuSTAR* in conjunction with X-ray observatories such as *Suzaku*, *XMM-Newton*, *Chandra*, and *Swift* to robustly constrain coronal and accretion disk properties in Seyfert galaxies.

This work was supported under NASA Contract No. NNG08FD60C and made use of data from the *NuSTAR* mission, a project led by the California Institute of Technology, managed by the Jet Propulsion Laboratory, and funded by the National Aeronautics and Space Administration. This research made use of the *NuSTAR* Data Analysis Software (NuSTARDAS) jointly developed by the ASI Science Data Center (ASDC, Italy) and the California Institute of Technology (Caltech, USA). M.L.K. gratefully acknowledges support through NASA grant #NNX13AE90G. G.M. and A.M. acknowledge financial support from Italian Space Agency under grant ASI/INAF I/037/12/0–011/13 and from the European Union Seventh Framework Programme (FP7/2007–2013) under grant agreement n.312789. C.S.R. acknowledges support from the NASA-ADAP program under grants NNX14AF86G and NNX14AF89G. F.E.B. acknowledges support from CONICYT-Chile (Basal-CATA PFB-06/2007, FONDECYT 1141218, Anillo ACT1101) and ICM grant IC120009, awarded to The Millennium Institute of Astrophysics, MAS. We thank Alan Marscher for helpful discussions. We thank the anonymous referee for comments, which have improved this manuscript. This research made use of Astropy, a community-developed core Python package for Astronomy (Astropy Collaboration et al. 2013), and Matplotlib (Hunter 2007).

*Facilities:* NuSTAR (FPMA, FPMB), Suzaku (XIS, HXD)

## APPENDIX
## INFLUENCE OF THE MINOR PILEUP IN SUZAKU XIS DATA

To investigate the influence of the mild pileup in the XIS data on our results, we extract XIS data from an annular region with inner radius 30″ and outer radius 170″. We fit our best-fit model to this data, and we find consistent parameter values within 90% confidence in one interesting parameter except for instrument cross-normalizations relative to XIS-FI. We find cross-normalizations for XIS-1 of $0.93 \pm 0.01$, PIN of $1.21 \pm 0.01$, FPMA of $1.00 \pm 0.01$, and FPMB of $1.03 \pm 0.01$. Thus, we find that the minor pileup fraction does not influence our conclusions on the spectral properties of NGC 4151.

## REFERENCES

Antonucci, R. 1993, ARA&A, 31, 473
Armentrout, B. K., Kraemer, S. B., & Turner, T. J. 2007, ApJ, 665, 237
Arnaud, K. A. 1996, in ASP Conf. Ser. 101, Astronomical Data Analysis Software and Systems V, ed. G. H. Jacoby, & J. Barnes (San Francisco, CA: ASP), 17
Astropy Collaboration, Robitaille, T. P., Tollerud, E. J., et al. 2013, A&A, 558, A33
Ballantyne, D. R., Ross, R. R., & Fabian, A. C. 2001, MNRAS, 327, 10
Beckmann, V., Shrader, C. R., Gehrels, N., et al. 2005, ApJ, 634, 939
Beckmann, V., Soldi, S., Ricci, C., et al. 2009, A&A, 505, 417
Beloborodov, A. M. 1999, ApJL, 510, L123
Bentz, M. C., Denney, K. D., Cackett, E. M., et al. 2006, ApJ, 651, 775
Berti, E., & Volonteri, M. 2008, ApJ, 684, 822
Boldt, E. 1987, PhR, 146, 215
Brenneman, L. 2013, Measuring the Angular Momentum of Supermassive Black Holes (New York: Springer)
Brenneman, L. W., Madejski, G., Fuerst, F., et al. 2014, ApJ, 788, 61
Brightman, M., Silverman, J. D., Mainieri, V., et al. 2013, MNRAS, 433, 2485
Cackett, E. M., Zoghbi, A., Reynolds, C., et al. 2014, MNRAS, 438, 2980
Chartas, G., Kochanek, C. S., Dai, X., Poindexter, S., & Garmire, G. 2009, ApJ, 693, 174
Dadina, M. 2008, A&A, 485, 417
Das, V., Crenshaw, D. M., Hutchings, J. B., et al. 2005, AJ, 130, 945
Dauser, T., Garcia, J., Parker, M. L., Fabian, A. C., & Wilms, J. 2014, MNRAS, 444, L100
Dauser, T., Garcia, J., Wilms, J., et al. 2013, MNRAS, 430, 1694
Dauser, T., Wilms, J., Reynolds, C. S., & Brenneman, L. W. 2010, MNRAS, 409, 1534
de Rosa, A., Piro, L., Perola, G. C., et al. 2007, A&A, 463, 903
de Vaucouleurs, G., de Vaucouleurs, A., Corwin, H. G., Jr., et al. 1991, Third Reference Catalogue of Bright Galaxies (Berlin: Springer)
Elvis, M. 2000, ApJ, 545, 63
Fabian, A. C. 2012, ARA&A, 50, 455
Fabian, A. C., Parker, M. L., Wilkins, D. R., et al. 2014, MNRAS, 439, 2307

Fabian, A. C., Rees, M. J., Stella, L., & White, N. E. 1989, MNRAS, 238, 729
García, J., Dauser, T., Lohfink, A., et al. 2014, ApJ, 782, 76
García, J., Dauser, T., Reynolds, C. S., et al. 2013, ApJ, 768, 146
George, I. M., & Fabian, A. C. 1991, MNRAS, 249, 352
Ghisellini, G., Haardt, F., & Matt, G. 2004, A&A, 413, 535
Grandi, P., & Palumbo, G. G. C. 2004, Sci, 306, 998
Haardt, F., Maraschi, L., & Ghisellini, G. 1994, ApJL, 432, L95
Harrison, F. A., Craig, W. W., Christensen, F. E., et al. 2013, ApJ, 770, 103
Holt, S. S., Mushotzky, R. F., Boldt, E. A., et al. 1980, ApJL, 241, L13
Houck, J. C., & Denicola, L. A. 2000, in ASP Conf. Ser. 216, Astronomical Data Analysis Software and Systems IX, ed. N. Manset, C. Veillet, & D. Crabtree (San Francisco, CA: ASP), 591
Hunter, J. D. 2007, CSE, 9, 90
Ives, J. C., Sanford, P. W., & Penston, M. V. 1976, ApJL, 207, L159
Jourdain, E., Bassani, L., Bouchet, L., et al. 1992, A&A, 256, L38
Kalberla, P. M. W., Burton, W. B., Hartmann, D., et al. 2005, A&A, 440, 775
Komatsu, E., Smith, K. M., Dunkley, J., et al. 2011, ApJS, 192, 18
Koyama, K., Tsunemi, H., Dotani, T., et al. 2007, PASJ, 59, 23
Kraemer, S. B., George, I. M., Crenshaw, D. M., et al. 2005, ApJ, 633, 693
Krolik, J. H., & Begelman, M. C. 1988, ApJ, 329, 702
Lubiński, P., Zdziarski, A. A., Walter, R., et al. 2010, MNRAS, 408, 1851
Magdziarz, P., & Zdziarski, A. A. 1995, MNRAS, 273, 837
Maisack, M., Johnson, W. N., Kinzer, R. L., et al. 1993, ApJL, 407, L61
Malzac, J., Beloborodov, A. M., & Poutanen, J. 2001, MNRAS, 326, 417
Marinucci, A., Matt, G., Kara, E., et al. 2014a, MNRAS, 440, 2347
Marinucci, A., Matt, G., Miniutti, G., et al. 2014b, ApJ, 787, 83
Markoff, S., Nowak, M. A., & Wilms, J. 2005, ApJ, 635, 1203
Martocchia, A., Matt, G., & Karas, V. 2002, A&A, 383, L23
Miller, L., Turner, T. J., & Reeves, J. N. 2009, MNRAS, 399, L69
Miniutti, G., & Fabian, A. C. 2004, MNRAS, 349, 1435
Miniutti, G., Fabian, A. C., Goyder, R., & Lasenby, A. N. 2003, MNRAS, 344, L22
Mitsuda, K., Bautz, M., Inoue, H., et al. 2007, PASJ, 59, 1
Mundell, C. G., Wrobel, J. M., Pedlar, A., & Gallimore, J. F. 2003, ApJ, 583, 192
Nandra, K., O'Neill, P. M., George, I. M., & Reeves, J. N. 2007, MNRAS, 382, 194
Nayakshin, S., & Dove, J. B. 2001, ApJ, 560, 885
Patrick, A. R., Reeves, J. N., Porquet, D., et al. 2012, MNRAS, 426, 2522
Pedlar, A., Howley, P., Axon, D. J., & Unger, S. W. 1992, MNRAS, 259, 369
Perola, G. C., Piro, L., Altamore, A., et al. 1986, ApJ, 306, 508
Piro, L., Nicastro, F., Feroci, M., et al. 1999, NuPhS, 69, 481
Puccetti, S., Fiore, F., Risaliti, G., et al. 2007, MNRAS, 377, 607
Radomski, J. T., Piña, R. K., Packham, C., et al. 2003, ApJ, 587, 117
Reis, R. C., & Miller, J. M. 2013, ApJL, 769, L7
Reynolds, C. S. 2013, CQGra, 30, 244004
Reynolds, C. S., Brenneman, L. W., Lohfink, A. M., et al. 2012, ApJ, 755, 88
Reynolds, C. S., & Fabian, A. C. 2008, ApJ, 675, 1048
Reynolds, C. S., & Nowak, M. A. 2003, PhR, 377, 389
Risaliti, G., Harrison, F. A., Madsen, K. K., et al. 2013, Natur, 494, 449
Ross, R. R., & Fabian, A. C. 1993, MNRAS, 261, 74
Sanfrutos, M., Miniutti, G., Agís-González, B., et al. 2013, MNRAS, 436, 1588
Schurch, N. J., Warwick, R. S., Griffiths, R. E., & Sembay, S. 2003, MNRAS, 345, 423
Shakura, N. I., & Sunyaev, R. A. 1973, A&A, 24, 337
Sim, S. A., Long, K. S., Miller, L., & Turner, T. J. 2008, MNRAS, 388, 611
Simkin, S. M. 1975, ApJ, 200, 567
Storchi-Bergmann, T., McGregor, P. J., Riffel, R. A., et al. 2009, MNRAS, 394, 1148
Svoboda, J., Dovčiak, M., Goosmann, R., & Karas, V. 2009, A&A, 507, 1
Takahashi, T., Abe, K., Endo, M., et al. 2007, PASJ, 59, 35
Tombesi, F., Cappi, M., Reeves, J. N., et al. 2011, ApJ, 742, 44
Ulrich, M.-H. 2000, A&ARv, 10, 135
Ulvestad, J. S., Wong, D. S., Taylor, G. B., Gallimore, J. F., & Mundell, C. G. 2005, AJ, 130, 936
Urry, C. M., & Padovani, P. 1995, PASP, 107, 803
Verner, D. A., Ferland, G. J., Korista, K. T., & Yakovlev, D. G. 1996, ApJ, 465, 487
Walton, D. J., Nardini, E., Fabian, A. C., Gallo, L. C., & Reis, R. C. 2013, MNRAS, 428, 2901
Walton, D. J., Risaliti, G., Harrison, F. A., et al. 2014, ApJ, 788, 76
Wang, J., Fabbiano, G., Elvis, M., et al. 2011a, ApJ, 736, 62
Wang, J., Fabbiano, G., Elvis, M., et al. 2011b, ApJ, 742, 23
Wilkins, D. R., & Fabian, A. C. 2011, MNRAS, 414, 1269
Wilms, J., Allen, A., & McCray, R. 2000, ApJ, 542, 914
Wilson, A. S., & Ulvestad, J. S. 1982, ApJ, 263, 576
Woo, J.-H., & Urry, C. M. 2002, ApJ, 579, 530
Yaqoob, T., Edelson, R., Weaver, K. A., et al. 1995, ApJL, 453, L81
Yaqoob, T., & Warwick, R. S. 1991, MNRAS, 248, 773
Yaqoob, T., Warwick, R. S., Makino, F., et al. 1993, MNRAS, 262, 435
Zdziarski, A. A., Johnson, W. N., & Magdziarz, P. 1996, MNRAS, 283, 193
Zoghbi, A., Fabian, A. C., Reynolds, C. S., & Cackett, E. M. 2012, MNRAS, 422, 129